A spatially-resolved transcriptional atlas of the murine dorsal pons at single-cell resolution

Stefano Nardone[1,2], Roberto De Luca[3,#], Antonino Zito[4,a,b,#], Natalie Klymko[5,#], Dimitris Nicoloutsopoulos[6], Oren Amsalem[1], Cory Brannigan[7], Jon M. Resch[8,9], Christopher L. Jacobs[1,2], Deepti Pant[1], Molly Veregge[1], Harini Srinivasan[1,2], Ryan M. Grippo[1], Zongfang Yang[1], Mark L. Zeidel[5], Mark L. Andermann[1], Kenneth D. Harris[6], Linus T. Tsai[1,2], Elda Arrigoni[3], Anne M. J. Verstegen[5,##,$], Clifford B. Saper[3,##,$], Bradford B. Lowell[1,##,$]

[1]Department of Medicine, Division of Endocrinology, Diabetes and Metabolism, Beth Israel Deaconess Medical Center and Harvard Medical School, Boston, MA, USA.
[2]Broad Institute of MIT and Harvard, Cambridge, MA, USA.
[3]Department of Neurology, Division of Sleep Medicine, Beth Israel Deaconess Medical Center and Harvard Medical School, Boston, MA, 02215, USA.
[4]Department of Twin Research & Genetic Epidemiology, King's College London, London, UK.
[5]Division of Nephrology, Department of Medicine, Beth Israel Deaconess Medical Center, Harvard Medical School, 330 Brookline Ave., Boston, MA 02215, USA.
[6]UCL Queen Square Institute of Neurology, University College London, London, UK.
[7]HEAVY.AI, 100 Montgomery St Fl 5, San Francisco, California, 94104, USA.
[8] Department of Neuroscience and Pharmacology, University of Iowa, Iowa City, IA, USA.
[9]Fraternal Order of Eagles Diabetes Research Center. University of Iowa Carver College of Medicine, Iowa City, IA 52242.

[#]Contributed equally.
[##]Contributed equally.
[$]Corresponding author.
Current address: [a]Department of Molecular Biology, Massachusetts General Hospital, Boston, MA, USA. [b]Current address: Department of Genetics, The Blavatnik Institute, Harvard Medical School, Boston, MA, USA.

ABSTRACT
The “dorsal pons”, or “dorsal pontine tegmentum” (dPnTg), is part of the brainstem. It is a complex, densely packed region whose nuclei are involved in the regulation of many vital functions. Notable among them are the parabrachial nucleus, the Kölliker Fuse, the Barrington nucleus, the locus coeruleus, and the laterodorsal, ventral, and dorsal tegmental nuclei. In this study, we applied single-nucleus RNA-seq (snRNA-seq) to resolve neuronal subtypes based on their unique transcriptional profiles and then used multiplexed error robust fluorescence in situ hybridization (MERFISH) to map them spatially. We sampled ~1 million cells across the dPnTg and defined the spatial distribution of over 120 neuronal subtypes. Our analysis identified an unpredicted high transcriptional diversity in this region and pinpointed many neuronal subtypes' unique marker genes. We also demonstrated that many neuronal subtypes found in mice were transcriptionally similar to those found in humans, enhancing this study's translational value. Finally, we developed a freely-accessible, GPU-powered interactive dashboard (http://harvard.heavy.ai:6273/) to provide access to this spatially-resolved transcriptional dataset.

INTRODUCTION
The pons consists of two main divisions: the “pontine tegmentum”, which represents its dorsal part, and the “basis pontis”, which is its ventral part. This study focuses on the dorsal portion of the pontine tegmentum (dPnTg). The dPnTg plays a pivotal role in the functioning of the autonomic nervous system, but it also represents a strategic hub for integrating many vital processes. It harbors many anatomically-defined subnuclei (abbreviations in Table 1) that perform a wide range of functions, including the parabrachial nucleus (PB) and locus coeruleus (LC), which have been implicated in receiving ascending visceral sensory and pain inputs from the spinal cord and medulla, and integrating them with forebrain cognitive, arousal, and emotional inputs to direct behavior, autonomic, and endocrine functions. In addition, specific neuronal populations residing in this area have been reported to be involved in respiration[1,2], arousal[3,4,5,6,7] sleep-wake regulation[8], pain[9,10], reward processing and reinforcement[11,12,13], movement[14,15], memory formation[16,17] feeding[18,19,20,21], micturition[22,23,24], aversive behaviors[25], thermoregulation[26,27], cardiovascular regulation[28], itch[29] and other behaviors. To facilitate future mechanistic investigations of how this brain region controls these processes, it is of great interest to catalog, at a transcriptional level, all the neuron subtypes that populate this area.

Although previous studies have identified genetic markers to selectively access some of the neuronal populations within the dPnTg, the field lacks a comprehensive transcriptionally and spatially-resolved neuronal map of this region. Here, we applied cutting-edge technologies in single-cell and spatial transcriptomics to unravel the neuronal complexity of the dPnTg[30,31]. To accomplish this, we first performed DroNc-seq, a single nuclei RNA-seq approach, on cells from this region. The purpose of this first step was two-fold: to identify highly informative marker genes specifying each neuronal subtype, which we would later use for spatial localization, and to obtain a complete transcriptomic inventory of genes expressed by the different neuronal subtypes. Then, MERFISH was performed using 315 informative genes to spatially locate each neuronal subtype within the dPnTg. In addition, because of the following factors: i) the increased sensitivity of MERFISH with regards to transcript detection, ii) the larger number of neurons profiled, and iii) the fact that we divided the dPnTg into 4 anatomical regions, these subsequent MERFISH studies helped to refine further, with increased granularity, the transcriptionally-defined neuronal subtypes that populate this brain region.

RESULTS
Single-nucleus transcriptional profiling identifies distinct cell types in the dPnTg

To profile the full transcriptome of the dPnTg at single-cell resolution, we employed DroNc-seq[30] (Fig 1a). To dissect our region of interest (ROI), i.e., the dPnTg, we first labeled the PB and the Bar, two brain nuclei that help define its extent, and then, we used their fluorescent signal to guide the dissection of the ROI (Fig 1b; see methods). We opted to perform single-nucleus instead of single-cell RNA-seq as the isolation of cells might alter gene expression and/or lead to the exclusion of cells due to their size or ability to survive the process. Of note, there is a high concordance between nuclear and cellular gene expression profiles in the brain[32,33,34]. However, a downside of profiling gene expression in nuclei is the reduced sequencing yield compared to single-cell approaches. To compensate for this limitation and increase the study's statistical power, we profiled 447,833 nuclei. After pre-processing and quality control steps, a dataset of 149,159 nuclei x 28,681 genes was analyzed using a pipeline that includes Seurat v.3.2.3 and Harmony v.1.0 packages[35,36,37,38] (SFig 1a-b; see methods).

Our analysis identified 41 clusters comprising 11 major cell types (Fig 1c-d; SFig 2a). Each cell type was characterized by uniquely expressed genes (i.e., markers), of which many have been previously reported in the literature (Fig 1e; SFig 2b; STable 1). Neurons encompassed 24 clusters, accounting for 60% of all nuclei (Fig 1c-d; SFig 2a). They expressed the pan-neuronal markers *Map2*, *Meg3,* and *Snap25* (Fig 1e; SFig 2b; STable 1). We also document four cerebellar clusters: those expressing *Itpr1*, *Pcp2*, and *Arhgef33* (cluster 12) were classified as Purkinje cells, and those expressing *Reln*, *Cadps2*, *Gabra6* (clusters 3, 15, 27) were classified as granule cells, as previously reported[39] (SFig 2c). The glial/ non-neuronal cells encompassed 17 clusters, accounting for the remaining 40% of all nuclei (Fig 1c-d; SFig 2a). We identified 10 major glial/ non-neuronal cell types: oligodendrocyte type I, expressing *Mag*, *Mog,* and *Enpp2*, and oligodendrocytes type II, expressing *Rplp1*, *Plekhb1*, and *Rps3,* along with high levels of *Mob*, *Mobp*, and *Fth1* (SFig 2b-c); astrocytes expressing *Slc1a2*, *Slc1a3,* and *Slc4a4*; oligodendrocyte precursor cells (OPCs) expressing *Pdgfra*, *Cspg4,* and *Tnr*; perivascular macrophages/microglia (PVMs/Micro) expressing *Tgfbr1*, *Siglech,* and *Hexb*; and vascular smooth muscle cells (VSMCs)/pericytes expressing *Rgs5*, *Slco1a4,* and *Ly6c1*. We also characterized two populations of vascular and leptomeningeal cells (VLMCs) defined by the expression of *Ranbp3l*, *Slc6a20a*, *Slc7a11* (VLMCs type I) versus *Slc47a1*, *Adamtsl3*, and *Mgp* (VLMCs type II), as previously reported[40]. Additional cell types identified were choroid plexus epithelial cells (CPE) marked by *Ttr* and *Tmem72* and ependymocytes marked by *Tmem212*, *Spef2*, and *Dnah12* (Fig 1c-e; SFig 2a-b; STable 1).

Neuronal clustering of the dPnTg reveals many novel populations

To disentangle the neuronal diversity of the dPnTg, we first selected all neurons, excluding cerebellar neurons and glial/ non-neuronal cells, and then categorized them into two main groups for re-clustering. The first group, called "excitatory neurons," included 35,861 nuclei divided into 33 clusters (Fig 1f). These neurons expressed *Slc17a6 (Vglut2)*, *Slc17a7 (Vglut1),* or *Slc17a8 (Vglut3),* marking them as neurons likely to release glutamate, and in some cases, they expressed *Th*/*Slc18a2* (noradrenergic neurons), *Tph2*/*Slc6a4* (serotoninergic neurons) or *Chat*/*Slc5a7* (cholinergic neurons) (Fig 1f, h). The second group, called "inhibitory neurons", included 24,526 nuclei divided into 29 clusters (Fig 1g). All neurons in this group expressed *Slc32a1* (*Vgat*) (which confers the ability to release GABA). At the same time, some also expressed *Slc6a5* (marking them as glycinergic neurons) or both *Vgat*/*Vglut2* (marking them as neurons that might release both GABA and glutamate – hence, "hybrid neurons")[41] (Fig 1g, i). Each cluster was defined by the expression of one or a combination of marker genes (Fig 1g-i; STable 2-3). Albeit to a different extent, nuclei from every experimental batch contributed to each neuronal cluster (% of cells), confirming the overlap between the two dissection strategies – one centered on the PB and the other on the Bar (SFig 2d left and middle plots). Sex was equally represented among the clusters (SFig 2d, right plot). Our analysis pinpointed numerous

novel neuronal populations and confirmed several already documented in the literature (Fig 1f-i; STable 2-3). We could identify even rare populations accounting for <1% of the dataset. Representative examples are *Qfrpr+*/*Nps+* neurons (cluster 29) mainly located at the borders of the nuclei of the lateral lemniscus (NLL) (at very far rostral LPB level), scattered throughout the PB or medial to the LC[42] and *Piezo2+/Anxa2+* neurons of the MTN, (cluster 32) a unique population of purely proprioceptive neurons in the brainstem[15].

MERFISH allows the identification and localization of distinct cell types in the dPnTg

We employed MERFISH to spatially resolve the transcriptional neuronal organization of the dPnTg (Fig 2a). Specifically, we examined the spatial expression profiles of a curated set of 315 genes that included: 1- highly variable genes obtained from differential expression (DE) analysis of the DroNc-seq dataset; 2- canonical glial, non-neuronal, and neuronal markers; 3- transcriptional factors, neuropeptides, and receptors – including those which could be potential pharmacological targets (STable 4; see methods). We profiled 5,664,695 cells across 46 coronal sections from 7 mice spanning, at intervals of 80-90 µm, a brain region corresponding to -4.7 to -5.8 bregma level in the Franklin-Paxinos atlas[43]. For each MERFISH section, we manually defined the boundaries of the ROI, i.e., the dPnTg. The dorsal boundary at rostral levels was defined by the inferior colliculus and more caudally by the dorsal surface of the pons; the ventral boundary was the dorsal part of the motor trigeminal nucleus (Mo5). Then, we used the boundaries' pixel cartesian coordinates to subset each gene count matrix to include only cells (*polygons*) and transcripts (*spots*) inside the ROI. After, we removed low-quality cells and retained 685,289 cells for downstream analyses (see methods). Throughout the manuscript, all mention of rostral to caudal bregma levels refers to sections matched to the Franklin-Paxinos atlas[43]. We also used the nomenclature from that atlas to identify nuclei and areas.

Our analysis of all cells from the ROI identified 44 clusters grouped into 9 transcriptionally distinct cell types (Fig 2b-c; SFig 7a; STable 5). Neurons encompassed 24 clusters, accounting for 50% of all cells in the dataset (Fig 2b-c; SFig 7a). Each cell type was characterized by uniquely expressed genes (Fig 2d; SFig 7b). Afterward, we selected only the neurons, discarded the cerebellar and glial/ non-neuronal clusters, and as before, divided them into two main groups for re-clustering. The first group, called "excitatory neurons", included 231,103 cells divided into 45 clusters (Fig 2e). Per our previous criteria, these neurons expressed either *Vglut1*, *Vglut2*, or *Vglut3,* marking them as glutamatergic neurons. In some cases, they expressed *Th*/*Slc18a2* (noradrenergic neurons), *Tph2*/*Slc6a4* (serotoninergic neurons), *Chat*/*Slc5a7* (cholinergic neurons), or *Slc17a6/Slc32a1* (also known as "hybrid neurons")[41] (Fig 2e, g). The second group, called "inhibitory neurons", included 110,332 cells divided into 45 clusters (Fig 2f). These neurons expressed *Vgat* (GABAergic neurons) or *Vgat*/*Slc6a5* (glycinergic neurons) (Fig 2f, h). Each cluster was defined by the expression of one or a combination of marker genes (Fig 2g-h; STable 6-7). Cells from different MERFISH slides belonging approximately to the same rostrocaudal level contributed equally to the same neuronal clusters (% of cells), confirming the reproducibility between independent series (SFig 7c middle and left plots). Sex was equally represented among the clusters (SFig 7c right plot). Supplementary Tables 8 ("excitatory neurons") and 9 ("inhibitory neurons") comprehensively list the neuronal MERFISH clusters, their marker genes, and spatial location.

Correspondence between MERFISH and DroNc-seq clusters of the dPnTg

Given the limited number of genes profiled by MERFISH, we sought to determine the degree to which clusters identified by MERFISH corresponded to DroNc-seq clusters. The rationale for applying this approach is that a 1:1 correspondence between MERFISH and DroNc-seq clusters would allow the inference of genes not probed by MERFISH from the DroNc-seq dataset. To this end, we applied MetaNeighborUS, an unsupervised replication framework that employs

neighbor voting to quantify the degree of cluster similarity across datasets while preserving the dataset independence[44,45]. In brief, cells from the reference dataset (e.g., MERFISH) vote for their closest neighbors in the target dataset (e.g., DroNc-seq), effectively ranking these cells by similarity. Then the cell-level ranking is aggregated at the cell-type level (i.e., clusters) in the target dataset as an area under the receiver operator characteristic curve (AUROC), which mirror the proximity of a target cell type to the reference cell type. The same analysis is computed by reversing reference and target roles. We considered only cluster-to-cluster correspondences with an AUROC >0.80 and/ or classified as "reciprocal" matches. We found that 72/90 MERFISH-identified clusters corresponded to 50/62 DroNc-seq-identified clusters, and this correspondence was reciprocal in 38/84 instances (Fig 2i-j; STable 10; see methods). In about half of the instances, more than one MERFISH cluster corresponded to a single DroNc-seq cluster. This is possibly due to the far larger number of neurons profiled and the higher MERFISH sensitivity in transcript detection (SFig 5b)[46,47], which lead to a better cluster granularity.

Clustering together all neurons from the dPnTg provides a general transcriptional portrait of the region, but it fails to separate neuron types whose transcriptional profiles are highly related. This problem stems from the fact that this entire region contains neurons whose transcriptome is highly diverse but, at the same time, harbors specific subnuclei whose neurons have a high degree of transcriptional similarity. The presence of transcriptionally diverse neurons from the broader PnTg region causes the transcriptionally similar neurons at the subnuclear level to cluster together. To overcome this issue and provide transcriptional resolution on a spatial scale that is of specific interest to investigators, we re-clustered the MERFISH-profiled neurons according to four anatomically defined subregions that include the following nuclei: 1) KF; 2) LPB and MPB; 3) MTN, pre-LC, LC, and Bar; and 4) LDTgV, LDTg, VTg, DTgC, DTgP, PDTg, CGA, CGB, Sph, O, and CGPn (see methods). In this study, we excluded from downstream analyses brain nuclei inside the ROI that were only partially represented in our sections as the DR, PPTg, SPTg, and others. To avoid ambiguity in the cluster nomenclature, we prepended a prefix to each cluster ID for each group (as identified above): "at1_", "at2_", "at3_", and "at4_" for subregion atlases 1, 2, 3, and 4, respectively.

MERFISH-resolved atlas of the KF

The KF, along with the LPB and MPB, is one of the three subdivisions of the parabrachial complex, a collection of subnuclei in the dorsolateral pons surrounding the superior cerebellar peduncle (*scp*)[48,49]. To achieve a finer granularity of the cell communities within each subdivision, KF and PB were analyzed separately. To build a transcriptional atlas of the KF, first, we bilaterally traced its boundaries on MERFISH coronal sections spanning from -4.8 to -4.9 bregma level, and then, we used their pixel cartesian coordinates to subset each gene count matrix to include only cells (*polygons*) and transcripts (*spots*) inside the defined boundaries (Fig 3a-b). A final dataset of 4,554 neurons was analyzed using our bioinformatic pipeline (see methods). This analysis pinpointed 19 clusters characterized by unique marker genes, which we classified into five groups based on shared gene expression profiles (Fig 3c, f). Briefly, group 1 includes clusters at1_0, at1_1, at1_6, at1_8, at1_14, and at1_17, and it is *Tfap2b*+; group 2 includes clusters at1_10 and at1_11, and it is *Calca*+/*Onecut3*+; group 3, the only GABAergic/ glycinergic group, includes clusters at1_4 and at1_13 and is *Pax2*+; group 4 includes clusters at1_7 (*Nos1*+/*Lhx9*+) and at1_15 (*Nps*+/*Qrfpr*+)[42,50], both located outside the KF along the margin of the NLL; lastly, the miscellaneous group includes clusters at1_2, at1_3, at1_5, at1_9, at1_12, at1_16, and at1_18, of which cluster at1_3 is located outside the KF (Fig 3b-c; STable 11). Group 1 accounts for 48.2%, group 2 for 9.4%, group 3 for 12.3%, and the miscellaneous group for 30.1% of KF neurons (Fig 3d). Next, to visualize neuronal clusters in space, we plotted the cartesian pixel coordinates of each cell as Voronoi plots and computed the cell frequency

(*cluster trajectory*) across three bregma levels, from -4.80 to -4.9 (Fig 3b, e). The four KF groups displayed distinct spatial distributions: group 1 neurons were found predominantly in the superior division and rostral part of the field; group 2 neurons were mainly in the ventral and caudal parts (cluster at1_10) or scattered across the KF (cluster at1_11); group 3 neurons were spread across all the KF; lastly, the miscellaneous group was found predominantly in the dorsal part of the field rostrally and in the more ventral part caudally (Fig 3b).

Interestingly, KF clusters at1_10 and at1_11, *Calca*+/*Onecut3*+, were segregated by *Pou6f2* and *Chst9* expression, respectively (Fig 3f, h). As *Calca*+ neurons are a well-known population of the LPBE[25,51,52], we wondered whether clusters at1_10 and at1_11 in the KF could be a more rostral continuation of that cell group. Therefore, we compared the transcriptome of the LPBE *Calca*+ neurons versus the one of *Calca*+ neurons of the KF. To test for a general transcriptional similarity, we performed a Pearson's *r* correlation among the average expression of 315 genes across all neurons of KF clusters at1_10, at1_11, and at1_6 (as a negative control, *Calca*-) and the PB cluster at2_2. Strikingly, the KF cluster at1_10 exhibited the highest correlation score (r= 84.8%) with PB cluster at2_2 compared to KF clusters at1_11 (r= 59.6%) and at1_6 (r= 33.3%) (Fig 3g). While cluster at1_11 is scattered, cluster at1_10 is focally concentrated in the ventral part of the KF and could represent a rostral continuation of the main *Calca*+ LPBE population (Fig 3i-j). To discover genetic markers that allow selective access to these neuronal subtypes, we performed a DE analysis between the PB cluster at2_2, all PB clusters except at2_2, and KF clusters at1_6, at1_10, and at1_11. *Calca* was expressed in KF clusters at1_10, at1_11, and PB cluster at2_2. *Onecut3* emerged as the most selective marker for KF *Calca*+ clusters at1_10 and at1_11 versus LPBE cluster at2_2. In addition, the genes *Ebf2* and *Chst9* selectively marked the KF cluster at1_11 (Fig 3h; STable 12). Anatomically, the KF clusters at1_10 and at1_11 mingle along their caudal edge with the most rostral neurons of the LPBE cluster at2_2. However, in immunohistochemical preparations, the KF *Calca*+ neurons stain less intensely for *Calca* and are smaller. In addition, the LPBE neurons project to the forebrain, whereas Huang et al. found a small projection to the ventrolateral medulla from PB complex neurons expressing Cre recombinase under the *Calca* promoter[53]. This projection likely comes from the neurons of clusters at1_10 or at1_11, a hypothesis that can now be tested as identifying distinct genetic markers will allow selective genetic access to these populations. Finally, a *Foxp2*+/*Slc17a6*+ neuronal population described by Geerling et al.,[54] likely corresponds to *Foxp2*+ clusters number at1_8 (also *Tfap2b*+/ *Foxp1*+/ *Rfxp1*+) and at1_9 (also *Tacr1*+) (Fig 3f).

MERFISH-resolved atlas of the PB

The other two divisions of the parabrachial complex are LPB and MPB[48]. To build a transcriptional atlas of the PB, first, we bilaterally traced its boundaries on MERFISH coronal sections spanning from -4.95 to -5.75 bregma level, and then we clustered the 79,413 neurons located within the PB boundaries using our bioinformatic pipeline (Fig 4a-b; see methods). The analysis identified 43 clusters, of which 38 belong indeed to the PB. The other 5 represent either glial contamination (at2_37) or originate from neurons of the paralemniscal nucleus (PL) (cluster at2_25), LDTg (clusters at2_30 and at2_38), and LC (cluster at2_39), respectively (Fig 4b). To gain a comprehensive spatial overview of the PB's cluster distribution, we plotted each cell's cartesian pixel coordinates as Voronoi plots and computed the *cluster trajectory* across nine sequential rostrocaudal levels. According to their spatial distribution, clusters were classified as rostral, caudal, or scattered (Fig 4a, c). We identified by DE analysis that each cluster was defined by the expression of one or more marker genes (Fig 4d; STable 13).

Next, we aimed to compare PB neuron types identified by this study with those described in the literature. We noted four different scenarios: 1- there is a close correspondence of the neuron

type location and marker gene between the two sources; 2- there is a correspondence between the neuron type location detected in our study and the one reported in the literature, but the marker gene has not been identified yet; 3- a neuron type reported in the literature lacked a neuron type in this study; or 4- a neuron type in our study lacked a correlate reported in the literature. Examples of a known neuronal population that has a correlate in our data would include cluster at2_2, *Calca+/Il20ra+,* which corresponds with the well-studied CGRP neurons in the LPBE (that are involved in response to aversive stimuli)[25]; cluster at2_5, *Foxp2+/Pdyn+*, which corresponds with dynorphin neurons located in the LPBD (that are involved in thermoregulation)[26,27]; and cluster at2_13, *Satb2+/Col14a1+*, which correspond to *Satb2* neurons located predominantly in the MPB (that are involved in taste perception)[55]. Examples of previously identified neuron types for which a marker gene had not been identified yet include the correspondence of the *Foxp2+/Slc32a1+* population in the MPBE[54] with GABAergic cluster at2_11, which also expresses *Foxp2*, but is marked more selectively by *Skor2* and *Gm47757.* This cluster differs substantially from another GABAergic population, cluster at2_16, which is *Foxp2-* and it is marked by *Slc6a5* and *Pax2,* which are expressed at high levels exclusively in the KF and at low levels in the MPBE (Fig 3f; SFig 8a-d; STable 14). Another example is cluster at2_9, *Rxfp1+/Runx1+*, which likely corresponds to *Cck+* neurons in the LPBS projecting to the ventromedial nucleus of the hypothalamus (VMH) and that are responsible for the control of counterregulatory responses to hypoglycemia[56]. Examples of neuronal populations reported in the literature but with no correlate in our study include *Oxtr+* cells, which regulate fluid intake[57]; *Tacr1+* cells, which regulate pain[10,9]; a *Pdyn+* population, which relays visceral and mechanosensory signals essential for meal termination[21] and a *Foxp2+/Pdyn-* cluster, located in an area that Geerling and colleagues called the rostral-to-external Lateral PB subnucleus (PBreL) that is activated at 4°C, as opposed to a *Foxp2+/Pdyn+* population of the LPBD (cluster at2_5) that is activated at 36°C[26,27]. Because these genes have been chosen for their correlation with a physiologically activated population of neurons, they might be co-expressed by more than one cluster rather than defining a single neuron type. We also found many neuron types and their marker genes lacking a previous description, especially in the MPB, where only a *Satb2+* neuron type was previously characterized (SFig 8e-f)[55]. Thus, given the region's complexity, we sought to give a comprehensive overview of all the PB clusters, including their location and markers, as data table (STable 15). To validate MERFISH reproducibility with an independent technique and as an example of a newly discovered group, we choose cluster at2_26. Its neurons express *Foxp2/Gpr101* (or *Trhr*) and are located in the part of the PB complex where Kaur et al. have found *Foxp2+/Calca-* neurons expressing *cFos* after animals are exposed to high CO_2[58]. This population, located adjacent to cluster at2_2 (*Calca+/Il20ra+*), is activated by hypercapnia and heavily projects to respiratory areas of the medulla[58]. Thus, it could correspond to cluster at2_26, as confirmed by the triple RNA-scope for *Foxp2*, *Pdyn*, and *Gpr101* (SFig 9a-c; STable 16-17). Unfortunately, *Foxp2* is not cluster-specific and cannot be used to access these neurons selectively. The two markers, *Gpr101* and *Trhr,* will permit genetic access to neurons in cluster at2_26 for future investigation.

Finally, we asked if a large population, such as cluster at2_2 (*Calca+/Il20ra+*), could harbor transcriptionally-defined subpopulations. To test this hypothesis, we isolated all 4,504 neurons from cluster at2_2, reran them through the same bioinformatic pipeline, and plotted the resulting cells using Voronoi plots. We included in the analysis only clusters composed of >200 neurons. Interestingly, each of the ten *Calca+* clusters is distinguished by different markers and has a specific spatial pattern (Fig 4e-h; STable 18). Clusters 4 (*Slc6a2+*) and 8 (*Qrfpr+*) were notable: the first is in the dorsal part of the main cluster at2_2, whereas the second is in its ventral part (Fig. 4i-j). Given the unique transcriptional profiles and spatial localizations of different subsets of *Calca* neurons, it is interesting to speculate whether these subsets subserve different aspects of functions previously attributed to the entire population of *Calca* neurons. It is also interesting

to speculate whether these different subsets of *Calca* neurons have different afferent and efferent connectivities.

Correspondence between MERFISH and scRNA-seq clusters from Pauli et al. in the PB
We aimed to reconcile our MERFISH classification of the PB neuronal types with that from Pauli et al. done using scRNA-seq[59]. To this end, we retrieved the processed DGEs and replicated the neuronal clustering reported in the manuscript. The dataset included 8,439 neurons grouped in 23 clusters specified by unique markers (SFig 10a-c; STable 19). Of these clusters, 21 were putative PB neurons, whereas the other two corresponded to glial contamination (cluster 23) and to a neuron type of the KF (cluster 16). Next, we used *MetaNeighborUS* function to assess the degree of cluster replicability between the two datasets[44,45]. We considered only cluster-to-cluster matches with an AUROC >0.85 and/ or classified as "reciprocal" hits (see methods). We found that 26/38 MERFISH-identified clusters corresponded to 19/21 scRNA-seq-identified clusters, and this correspondence was reciprocal in 14/31 instances (SFig 10d-e; STable 20; see methods). While ~90% of scRNA-seq clusters corresponded with a MERFISH cluster, the opposite was true only for ~70% of MERFISH clusters. These "unmatched" MERFISH clusters could represent clusters not resolved by scRNA-seq technology or missed by the dissection strategy. In addition, we confirmed two *Calca*+ populations found by Pauli and colleagues: a high-expressing *Calca* population (cluster 15), corresponding to the LPBE cluster at2_2 (AUROC=0.95), and a medium-expressing *Calca* population (cluster 16), possibly corresponding to the KF cluster at1_11. To test this hypothesis and confirm the genes distinguishing the main KF (at1_11) and PB (at2_2) *Calca*+ populations identified previously by DE analysis (Fig 3h), we performed a DE analysis between clusters 15 and 16 of the Pauli et al. dataset. Strikingly, among the top-scoring differentially expressed genes, the same genes were identified by our previous analysis (SFig 10f-g; STable 21). Combining the data from these studies strengthens our findings and gives a complete overview of most PB neuron types of transcriptomes, spatial locations, and projections.

MERFISH-resolved atlas of the MTN, pre-LC, LC, and Bar: *focus on MTN and LC*
Next, we focused on the MTN and LC. To build a transcriptional atlas of a ROI that includes MTN, LC, pre-LC, and Bar, first, we bilaterally traced its boundaries on MERFISH coronal sections spanning from -5.2 to -5.8 bregma level, and then we clustered the 22,358 neurons within the ROI boundaries using our bioinformatic pipeline (Fig 5a-b; see methods). Overall, we detected 30 clusters, of which only 25 correspond to neurons of this ROI. The other 5 are likely glial contamination (clusters at3_4, at3_6, at3_20, and at3_21) or cholinergic neurons from the LDTg (cluster at3_29). Each cluster was characterized by unique gene expression and spatial patterns (Fig 5a-d; STable 22). Based on their anatomical location, we divided them into three groups: group 1 includes clusters of the lateral region, including the MTN, LC, and pre-LC; group 2 includes clusters exclusive to the medial region, including the Bar; group 3 includes clusters whose cells were spread across both regions (Fig 5a, c).

The MTN is a paired structure located at the mesopontine junction, which conveys information about jaw closure to brainstem sites related to chewing. It consists of two populations of primary proprioceptive trigeminal sensory neurons that ipsilaterally innervate spindles in the jaw-closing muscles (*first population*; 80–90% of all MTN neurons) or periodontal pressure receptors (*second population*; 10–20% of all MTN neurons)[60]. We identified clusters at3_8 and at3_24 as MTN neurons because of their unique spatial organization and the expression of *Prph*, *Slc17a7*, and *Pvalb* (Fig 5e)[15]. Most probably, cluster at3_8 (79% of all MTN neurons) corresponds to the first, most abundant MTN population that innervates muscle spindles, whereas cluster at3_24 (21% of all MTN neurons) to the second, less abundant population that innervates periodontal tissue. Besides confirming similar expression levels of *Prph, Slc17a7, and Pvalb* between the

two clusters (adj. p-value >0.01), by performing DE analysis, we also identified unique marker genes for cluster at3_8, e.g. *Rnf220*, *Ebf1*, *Gpr156* and cluster at3_24, e.g. *Brs3*, *Cd36*, *9630002D21Rik (*adj. p-value <0.01*)* (Fig 5e; STable 23) that will allow studying their different properties.

The LC is a nucleus located in the dorsolateral PnTg on the lateral floor of the fourth ventricle and represents the primary source of noradrenergic innervation of the cerebral cortex and cerebellum[3,4]. It receives input from widespread brain regions and projects throughout the forebrain, brainstem, cerebellum, and spinal cord[4]. Recently, it has been demonstrated that the modular input-output organization of the LC can enable temporary, task-specific modulation of different brain regions[4]. However, whether this modularity corresponds to transcriptionally-defined groups of noradrenergic neurons is still undetermined. To this end and to obtain better granularity, we isolated 4,074 noradrenergic neurons from cluster at3_0, reran them through the same bioinformatic pipeline, and plotted the resulting cells using Voronoi plots and *cluster trajectory* (Fig 5g-i). We included only clusters with >200 neurons in the analysis. Each cluster was distinguished by different markers and had a specific spatial pattern (Fig 5g-j; STable 24). Clusters 0, 1, 4, and 5 were distributed across the LC. In contrast, cluster 2 (*Col18a1*+/*Gpr101*+) was located in the dorsal portion of the caudal LC, and cluster 3 (*Tacr3*+/*Ecel1*+) in the ventral part of the rostral LC (Fig 5g, i). As cortical projections arise mainly from the dorsal LC and spinal projections from the ventral LC, it would be interesting to determine whether these populations have different targets[61,62]. In addition, we report that the LC contains two non-noradrenergic neuronal populations. The first is a scattered population of somatostatin neurons expressing low *Vgat* and *Vglut2*. (Fig 5d). These neurons likely correspond to cluster at3_10 of the main clustering and differ from somatostatin neurons of cluster at3_28, which are *Vglut2*-, *Vgat*+, and *Npy*+ and are located along the ventral edge of Bar. (Fig 5d). The second is a scattered population of *Penk* neurons that is part of cluster at3_1 of the main clustering (Fig 5d).

MERFISH-resolved atlas of the MTN, pre-LC, LC, and Bar: *focus on pre-LC and Bar*

The term “pre-locus coeruleus” refers broadly to a small region that lies on both sides of the LC, approximately from levels -5.3 to -5.7 in our parcellation. Like the LPB, the pre-LC receives inputs from the nucleus tractus solitarii (NTS) and the paraventricular hypothalamus (PVH) and sends efferent projections to the thalamus and multiple hypothalamic sites[63]. This raises the possibility that the pre-LC shares functions with the LPB. Recently, Li et al. identified an afferent input from the PVH-*Pdyn*+ neurons that regulates food consumption[20]. However, the molecular identity of various pre-LC neurons remains uncharacterized. Our analysis detected six clusters restricted to the pre-LC (group 1 except clusters at3_0, at3_8, and at3_24) and another seven whose cells were shared with medial regions (group 3) (Fig 5a-b). To date, the only well-defined group of pre-LC neurons has been described by Geerling et al. on the basis that they: 1) receive excitatory inputs from aldosterone-sensing HSD2 neurons of the NTS [64,65,66]; 2) express *Foxp2* and *Pdyn* genes[63], and 3) express elevated levels of *cFos* during dietary sodium deprivation[67]. Based on their gene expression, the pre-LC neurons described by Geerling and colleagues could correspond to our cluster at3_30, *Tnc*+/*Rxfp2*+. Strikingly, both clusters at3_30 in this atlas and at2_5 from the PB atlas are *Foxp2*+/*Pdyn*+ and send efferent projections to the same brain regions, the preoptic area (PoA) and hypothalamus[63,68]. Both salt deprivation (which activates at3_30) and elevated external temperature (which activates at2_5) require consumption of salt and water, which are mediated by the median preoptic nucleus (MnPO)[69]. To explore for marker genes that would allow selective access to one cluster versus the other, we performed a DE analysis between them. Besides finding similar average expression levels for *Foxp2*, *Pdyn,* and *Th* between the two clusters, we also identified the top 5 (adj. p-value

<0.01) marker genes for cluster at3_30. Of note, none of the genes in our MERFISH panel was a marker for PB cluster at2_5 (Fig 5f; STable 25).

The Bar is a small nucleus between the LC and the LDTg and is critical for bladder voiding behavior[22,70]. Electrical or pharmacological activation of this region triggers micturition, i.e., urination[71]. Bar neurons fulfill their task through long-range projections to the lumbosacral level of the spinal cord[72,24], where parasympathetic motor neurons that innervate the bladder and inhibitory interneurons connecting to sphincter motor neurons reside. While more than half of Bar's spinally projecting neurons express *Crh* as a peptidergic neurotransmitter[73], (and when activated, these promote bladder contractions), the genetic and functional identity of other Bar neurons remains elusive. Our analysis detected nine clusters in the medial region (group 2). Cluster at3_2, which expresses *Crh/Oxtr*, is the main glutamatergic (*Vglut2*+) population (Fig 5a-c). Other glutamatergic clusters with cells located in or near Bar are clusters at3_9 (*Lhx4*+/*Vsx2*+), at3_26 (*Vglut3*+), and at3_1 (*Penk*+/*Mc4r*+) (Fig 5a-d). It was recently shown that photo-inhibition of Bar^{Esr1} neurons terminates ongoing urethral sphincter relaxation and stops voiding[74]. *Esr1* transcript was detected in neurons of cluster at3_2 (*Crh+/Oxtr+)* and to a lower extent in cells of other Bar clusters (SFig 9d). Hence, Esr1 expression is not specific to one neuronal population in Bar. Among the GABAergic populations, cluster at3_12 (*Crhbp*+/*Glp1r*+) is intermingled with the *Crh*+ neurons rostral to the core of Bar, whereas GABAergic clusters at3_25, at3_27, at3_28, and at3_31 surround the nucleus. Since Bar neurons are under GABAergic control[75], these inhibitory populations could represent neurons in the CGPn or local interneurons that influence the Bar's neuronal activity. Furthermore, Bar neurons have extensive dendritic arbors[24], and cholinergic neurons in LDTg (cluster at3_29) are likely in close contact with the *Crh*-positive neurites[76].

MERFISH-resolved atlas of the brain nuclei of the medial part of the dPnTg

To investigate a ROI that includes LDTg, VTg, DTg, CGA, CGB, Sph, O, and CGPn, we first traced its boundaries on MERFISH coronal sections spanning from bregma level -4.7 to -5.8, and then we clustered the resulting 120,182 neurons within the ROI boundaries using a custom bioinformatic pipeline (Fig 6a-b; see methods). Overall, we detected 46 clusters, of which only 37 corresponded to neurons of this ROI. The other 9 were likely glial contamination (clusters at4_2, at4_8, at4_14, at4_39, at4_43, at4_44, and at4_45) or originated from nearby brain nuclei, such as the DR (cluster at4_26) or LC (cluster at4_33). Each cluster was characterized by its unique gene expression and spatial patterns (Fig 6a-d; STable 26). According to the *cluster trajectory,* calculated across 11 sequential rostrocaudal levels, we classified the clusters as rostral, central, or caudal (Fig 6c).

The LDTg is one of the major sources of acetylcholine in the pons. It borders the LC and the DTg through some of its course from bregma level -4.7 to -5.6[77]. To unravel its neuronal complexity, we first computed the overall contribution of each cluster to the LDTg/ LDTgV and then its trajectory across 11 rostrocaudal levels (Fig 7b-c). We included only clusters contributing >0.5% to the overall LDTg/ LDTgV neuronal population. Our analysis detected 27 LDTg/ LDTgV neuronal clusters, of which 17 (55%) are GABAergic, 8 (32%) are glutamatergic, and 2 (13%) are cholinergic (Fig 7b). Our data in mice are in line with Luquin E. et al., who documented the coexistence of GABAergic (*GAD65/GAD67+; 39.8%*), glutamatergic (*Vglut2+; 31.5%*), and cholinergic (*ChAT+; 22.2%*) neurons in the rat LDTg (Fig 7d, left side)[78].
The cholinergic neurons are a well-characterized neuronal population of the LDTg active during wakefulness and REM sleep[79]. They cannot release glutamate and GABA[78], as in the case of clusters at4_1 and at4_39 of this dataset that lack *Vglut2* and *Vgat* expression (Fig 6d). Among the glutamatergic clusters, *Shox2*+ clusters at4_0 and at4_7 (also *Lhx4*+) represent most of the *Vglut2*+ cells and are distributed uniformly from rostral to caudal, where they gradually replace

the cholinergic population. The remaining *Vglut2*+ clusters (at4_22, at4_ 23, at4_28, at4_31, and at4_32) are primarily rostral (Fig 7b-c). Interestingly, cluster at4_28 (*Tnc*+) is only found in the LDTgV, representing a potential marker to study its specific function[80] (Fig 7a). Conversely, GABAergic clusters show a marked spatial distribution along the rostrocaudal axis (Fig 7b-c). Besides Chat+ neurons, the only other well-characterized neuronal population of the LTDg is marked by *Vgat*/*Glp1r. Glp1r* neurons play a role in attenuating cocaine-seeking behavior by projecting to the ventral tegmental area (VTA)[81]. We found *Glp1r*+ cells in GABAergic clusters at4_21 and at4_38 and the glutamatergic cluster at4_22. In addition, the percentage of *Vgat*+/*Glp1r*+ versus *Vglut2*+/*Glp1r*+ cells is concordant between this and Hernandez et al. study in mice (Fig 7d, right side)[81]. This further validates our analyses.

Gudden's tegmental nuclei comprise two distinct divisions: VTg and DTg. In the rat, both divisions send heavy projections to the mamillary bodies: the VTg innervates the medial mammillary nucleus supporting spatial learning by generating medial mammillary theta waves, whereas the DTg innervates the lateral mammillary nucleus, supporting navigation through its influence upon the head direction system[17,82].
The VTg is located near the midline from -4.7 to -5.2 bregma level and is a pure GABAergic nucleus (Fig 7e-f). From our analyses, we determined that >90% of its neurons belong to GABAergic cluster at4_6 (*Satb1*+), while the remaining are from clusters at4_4 (*Tacr1*+), at4_38 (*Robo3*+) and at4_40 (*Calca*+) (Fig 7f). The DTg is also located near the midline, from -5 to -5.8 bregma level, and it is composed of three divisions: the DTgP, DTgC, and PDTg (Fig 7g). Its primary function is in landmark and directional navigation. Its cells, referred to as head direction (HD) cells, are believed to encode the animal's perceived directional heading with respect to its environment[14]. In fact, they fire in response to changes in head velocity and direction (i.e., left, right)[14]. Thus, we expect a fine-tuned functional organization to correspond to a highly compartmentalized cell distribution. To decrypt its spatial organization, we first computed the overall contribution of each cluster to the DTg and then its trajectory across 10 sequential rostrocaudal levels (Fig 7h-i). We included only clusters contributing >0.5 % to the overall DTg neuronal population. Our analysis identified 21 clusters, which we divided into GABAergic (17/21 clusters, representing 88.5% of DTg neurons) and glutamatergic (4/21 clusters, representing 11.5% of DTg neurons) (Fig. 7h). Next, we investigated their spatial location with respect to their anatomical organization. The DTgP extends from bregma level -5 to -5.6 (Fig 7g). The rostral-central part of the DTgP is mainly characterized by GABAergic clusters at4_3 (*Vmn1r209*+), at4_5 (*Gpr39*+), at4_12 (*Nts*+), and at4_16 (*Onecut1*+) (Fig 7i, k). In contrast, its caudal part is mostly glutamatergic and harbors cluster at4_0 (*Shox2*+) and a small GABAergic *Npy*+ population corresponding to cluster at4_36 (Fig 7i, k). The DTgC borders the DTgP for all its extension, except in its very rostral part (Fig 7g). The rostral-central part of the DTgC is populated exclusively by the GABAergic cluster at4_4 (*Tacr1*+) that ends in the caudal region, intermingled with the glutamatergic cluster at4_25 (*Lhx9*+) (Fig 7k). Finally, the PDTg occupies the very caudal portion of the DTg, from -5.70 to - 5.80 bregma level (Fig 7g). It represents a point where VTg, DTgP, DTgC, and the Sph converge into one structure. Thus, from a compartmentalized spatial distribution, the DTg culminates into a mixture of cells from the abovementioned nuclei (Fig 7k). Dorsal to the DTgP from -5.4 to -5.55 bregma level, there is the Sph. Our analyses indicated that it is composed of >90% of GABAergic neurons belonging to clusters at4_18 (*Ebf2*+) and at4_41 (*Rxfp1*+) (Fig 7j).

Finally, we examined the nucleus O (also known as NI), CGA, and CGB. The "nucleus incertus" (NI) extends from -5.30 to -5.6 bregma level and consists of a midline, bilateral cluster of large, multipolar neurons in the central grey[6] (Fig 7g; SFig 12 c). "Incertus", in Latin, means "uncertain", alluding to its "unknown" function; however, recent evidence suggests its involvement in modulating arousal, feeding, stress responses, anxiety, addiction, attention, and

memory by projecting to high-order structures of the forebrain[5,7,16]. Despite its main GABAergic population being known to express *Rln3*, the genetic makeup of the other neuronal subtypes is unknown. As before, we first computed the overall contribution of each cluster to the NI, CGA, and CGB brain nuclei and then its trajectory across 5 sequential rostrocaudal levels (SFig 12a-c). We included only clusters contributing >0.5% to the overall NI, CGA, and CGB neuronal populations. In this ROI, our analysis identified 24 neuronal clusters, of which 16 (58.2%) are GABAergic and 8 (41.8%) are glutamatergic (SFig 12a). None of the clusters was characterized by a specific spatial pattern along the rostrocaudal axis but were spread across the entire area (SFig 12b).

Comparison between mouse and human neuronal subtypes reveals a high degree of transcriptional similarity

A recent preprint from Siletti et al.[83] made snRNA-seq data from the human pons accessible. Specifically, we retrieved all the nuclei collected from two dissection approaches: the first including the pontine reticular formation (PnRF) and the PB; the second, the DTg and all other medial nuclei in the dPnTg. A pre-filtered dataset of 24,977 high-quality nuclei x 35,003 genes was analyzed using a bioinformatic pipeline that includes Seurat v.3.2.3 and Harmony v.1.0 packages (see methods)[35,36,37,38]. The analysis identified 29 clusters that we grouped into 10 main cell types (Fig 8a-b; SFig 11a-b; STable 27). Regional cell type composition and marker genes were highly similar between mouse and human species (Fig 1c-d, 8b-c). Next, we isolated only the neurons, excluded the cerebellar and the glial/ non-neuronal clusters, and divided them into two main groups for re-clustering (Fig 8d-e; SFig 11c). The first group, called “excitatory neurons”, included 8,632 nuclei divided into 29 clusters (Fig 8d). Per our previous criteria, this group included neurons expressing either *VGLUT1*, *VGLUT2*, or *VGLUT3,* marking them as glutamatergic neurons or, in some cases, *TH*/*SLC18A2* (noradrenergic neurons), *TPH2*/*SLC6A4* (serotoninergic neurons) or *CHAT*/*SLC5A7* (cholinergic neurons) (Fig 8d, f). The second group, called “inhibitory neurons”, included 6,221 nuclei divided into 23 clusters (Fig 8e). These neurons expressed *VGAT* (GABAergic neurons), *VGAT*/*SLC6A5* (glycinergic neurons), or *VGLUT2*/*VGAT* (hybrid neurons)[41] (Fig 8e, g). Each cluster was defined by the expression of one or a combination of marker genes (Fig 8f-g; STables 28-29). Albeit to a different extent, every donor contributed to each neuronal cluster (% of cells), confirming the mitigation of the batch effect (SFig 11d-h).

Next, given the extensive use of mus musculus as a model to study neuronal circuits and mechanisms underlying specific human behaviors, we sought to evaluate the degree of transcriptional similarity between human and mouse neuron types of the dPnTg. We employed the unsupervised MetaNeighborUS function by applying the following criteria: only cluster-to-cluster matches with an AUROC >0.85 and/ or classified as “reciprocal” hits were included (see methods). Strikingly, we found that 33/52 human snRNA-seq clusters corresponded to 28/62 mouse DroNc-seq clusters, and the correspondence was mutual in 23/38 instances (Fig 8h-i; STable 30). This result indicates that about half of the dPnTg clusters have a high degree of transcriptional similarity across the two species (Fig 8i). This fact could underlie a conserved function across species. Finally, to gain more insights into the functionality of genes driving cell-type replicability, we applied a supervised MetaNeighbor function that requires clusters with “reciprocal’ matches and a list of gene sets to test. As gene sets, we used the *mus musculus* gene ontology (GO). In this analysis, each AUROC mirrors the performance of individual gene sets, that is, how well an individual GO gene set contributes to each cell type's replicability. The average AUROC, instead, indicates the global performance of a GO gene set across all the cell types tested (see methods). The top 10 scoring average AUROCs pinpointed GO terms related to neurotransmitters and synaptic functions (top average AUROC ~0.8) (Fig 8j-k; SFig 13a; STable 31). This means these GO gene sets are moderately conserved functional gene

ensembles contributing to cell-type replicability between the two species. Of interest, neuropeptides-related GO terms were also moderately conserved but with a lower score (top average AUROC ~0.7) (SFig 13b; STable 31).

To rule out the possibility that similar clusters might originate from anatomically different parts of the dPnTg and to gain further granularity in a region of great interest, we decided to focus on the PB for three key reasons: first, the PB has conserved anatomy between human and mouse species; second, we generated a detailed transcriptional atlas of this region in mice; and third, the PB was precisely dissected in human, allowing us to select only those nuclei belonging to PnRF and PB dissections[83]. After discarding the GABAergic clusters to limit the contamination from neighboring areas, a dataset of 3,384 putative PB human neuronal nuclei was re-analyzed. The analysis identified 24 clusters specified by distinct marker genes (Fig 8l-m; STable 32). Remarkably, MetaNeighbor analysis ran between the mouse DroNc-seq "excitatory neurons" (after excluding non-PB clusters 9-10, 15, 19-20, 25-26, 30, 32) and the human snRNA-seq neuronal datasets of the PB revealed that many of the mouse PB clusters had a high degree of similarity with human PB clusters. Among them, there were clusters 0 (*GLP1R*/*PAX5*), 4 (*CALCA*/*CALCB*), 10 (*DDR2*/*CHST9*), 12 (*SATB2*/*EDENRB*), 18 (*NPY*/*VIPR2*), 19 (*TBL1Y*/*LHX2*), 14 (*LINC00540*/*P2RY1*), and the *FOXP2*+ clusters1 (*TH*+), 5 (*GPR101*+) and cluster 21 (*NPS*+) (STable 33). Clusters 5 and 12 had an AUROC of 0.81 and 0.84, respectively, but were listed because they were biologically meaningful. Of note, clusters 4 and 21 have been confirmed by immunohistochemistry in sections of human post-mortem brain tissue[84,85]. For cluster 4, the human CGRP cell group is in the same relative location as the LPB *Calca* neurons in mice, and CGRP terminals were found in the same forebrain areas that are targeted by CGRP neurons in rodents. Overall, our results confirm the value of using *mus musculus* as a model to study human brain mechanisms underlying specific behaviors.

MERFISH and DroNc-seq data visualization

We developed a freely-accessible, GPU-powered, interactive dashboard providing access to this extensive resource of spatially-resolved transcriptional data at single-cell resolution. This enabled us to display the vast amount of generated data, which would not have been feasible with static, conventional graphics. The visualizer allows for targeted, precise exploration of the MERFISH spatial data across the entire dPnTg region. A powerful aspect of the visualizer is its built-in analytical functions which enable the user to perform analyses within the visualization itself. The dashboard produces advanced visualization and analytics of big data by harnessing the massive parallelism of modern GPU and CPU hardware.

We plotted 14 representative coronal sections on the dashboard, spanning our ROI from -4.7 to -5.80 bregma level at 90-80 µm intervals. In addition, as described in the manuscript, we divided the dPnTg into 4 anatomical subregions. To query each subregion separately, 4 different atlases were added to the dashboard (see methods). Atlases representing subregions 1 (KF) and 2 (PB) are displayed on one page, as both are part of the parabrachial complex. The dashboard is accessible at: http://harvard.heavy.ai:6273/.

We also plotted all our cluster analyses that include data from DroNc-seq and MERFISH on the single-cell BROAD portal. Besides the interactive visualization, the platform performs DE analysis and real-time plotting of both features and cells. The viewer is accessible at: https://singlecell.broadinstitute.org/single_cell/study/SCP1808.

DISCUSSION

To gain selective access and mechanistically investigate the neuronal subtypes within the dPnTg, it is necessary to identify their spatial distribution and transcriptional identity, particularly their marker genes. While the field presently has characterized some genetic markers for this

region, the transcriptional identity of most neuronal subtypes has remained elusive. By combining DroNc-seq and MERFISH, we generated a spatially-resolved transcriptional atlas of the dPnTg at a single-cell resolution. This study analyzed ~1 million cells and identified over 120 neuronal clusters across 4 anatomical subregions of the dPnTg. To accomplish this, we employed an unsupervised approach, DroNc-seq, to identify the most informative genes and then a supervised approach, MERFISH, relying on a subset of 315 genes, to spatially resolve the neuronal clusters. Despite the lower number of genes probed, MERFISH's higher sensitivity, and the significant number of neurons profiled, coupled with the possibility of subsetting smaller regions than those obtained by tissue microdissection, lead to a finer cluster granularity than the DroNc-seq approach. To compare DroNc-seq and MERFISH datasets, we did not opt for a computational integration because the two approaches have systematically different statistics at the transcript level that hamper efficient harmonization[86]. Therefore, we applied MetaNeighborUS, an unsupervised replication framework that employs neighbor voting to quantify the degree of cluster similarity across datasets while preserving the dataset independence[44,45]. Mapping the correspondence between clusters using MetaNeighborUS allows transferring transcriptional and spatial information from one dataset to another.

To our knowledge, this is the first study to spatially characterize the transcriptome of the mouse dPnTg at single-cell resolution. For the first time, we identified the neuronal subtypes populating this region, spatially located them and provided the marker genes that specify each subtype. In addition, we related this information to the scientific literature to reconcile our findings with the field's current state of knowledge. Our spatially-resolved transcriptional atlas should greatly facilitate future mechanistic investigations of neural circuits in this region. For example, knowing the genetic markers allows for designing recombinase-driver mice that can be used to access specific neuronal populations to perform behavioral, neuronal tracing, and activity mapping experiments[87,88]. In addition, we have created a GPU-powered visualizer which allows scientists to interactively interrogate our spatially-resolved datasets, which includes a representative series of 12 sequential coronal sections cut at intervals of 80-90 µm that span rostrocaudal bregma levels from -4.7 to -5.8.

Finally, this study explores the degree of transcriptional similarity between dPnTg neuronal clusters identified in mice compared to humans. Strikingly, half of the dPnTg neuronal clusters were transcriptionally similar between the two species. These results may have broad implications for translational research targeting this region, given the extensive use of the mouse as a model to study neuronal circuits and mechanisms underlying specific human behaviors and physiology. By leveraging these two molecular techniques, we built a spatially-resolved transcriptomic atlas of the dPnTg at single-cell resolution and made the dataset accessible and interactive. This will allow future studies to shed light on the function of the many neuronal subtypes populating this region.

ONLINE METHODS

Mouse strains and brain dissections

DroNc-seq and MERFISH experiments were performed on C57BL/6J background mice purchased from the Jackson Laboratory (JAX). Mice were housed at 25°C, ~55% humidity, on a 12:12-h light/dark cycle. Animal experiments were approved by the Beth Israel Deaconess Medical Center's Institutional Animal Care and Use Committee (IACUC) (protocol no. 047-2022). A total of 9 and 8 batches (3-5 mice each) of male and female mice, respectively, 8-10 weeks old, were used for DroNc-seq. To obtain a more precise dissection of the dPnTg and minimize the contamination from neighboring areas, such as the cerebellum, we labeled two nuclei that define its extension: the PB and the Bar.

To visualize the PB, we exploited the fact that the PB receives extensive synaptic inputs from the NTS[89]. A Cre-expressing adeno-associated virus, AAV1-hSyn-Cre (*pENN-AAV1-hSyn-Cre-WPRE-hGH*; titer ≥ 1×10^{13} vg/mL; Addgene, 105553), was injected into the NTS of an Ai14 mouse. The Ai14 mouse (JAX, stock no. #007914, Gt(ROSA)26Sor$^{tm14(CAG\text{-}tdTomato)Hze}$) has a Cre reporter allele with a loxP-flanked STOP cassette preventing transcription of a CAG promoter-driven red fluorescent protein variant (tdTomato), all inserted into the Gt(ROSA)26Sor locus. Injection of AAV-Cre into the NTS results in the expression of tdTomato, which travels through the projections from the NTS to label the PB specifically. Two weeks after the AAV injection, mice were decapitated for brain dissection. To visualize the Bar, we exploited the highly selective expression of *Crh* in this brain nucleus[24]. Crh-IRES-Cre mice (JAX, stock no. #012704, B6(Cg)-Crh$^{tm1(cre)Zjh/J}$) were crossed with EGFP-L10a (JAX, stock no. #024750, B6;129S4-Gt(ROSA)26Sor$^{tm9(EGFP/Rpl10a)Amc/J}$) to obtain Crh-IRES-Cre::EGFP-L10a mice whose *Crh*-expressing neurons were selectively labeled with GFP.
In both approaches, mice were sacrificed between 10 am -1 pm. To avoid any stress-related transcriptional changes, mice were decapitated immediately after removal from home cages. After decapitation, the brain was removed from the skull, chilled for 3 min in an ice-cold DMEM/F12, no phenol red (Thermo Fisher Scientific) media slush, and placed ventral surface up in an ice-cold stainless steel brain matrix (Roboz Surgical Instrument Co). A coronal slice of 1 mm thick was cut, and the area of interest was dissected bilaterally using a micro dissecting knife (Roboz Surgical Instrument Co.) under the fluorescent stereotactic microscope (Zeiss Discovery V8). Dissections were flash-frozen in dry ice and stored at -80°C.

Stereotactic injection into the NTS
Stereotaxic AAV injections into the NTS were performed in seven- to ten-week-old male mice under ketamine (100 mg/kg) and xylazine (10 mg/kg) anesthesia. Mice were placed into a stereotaxic apparatus (David Kopf model 940) with the head angled down at approximately 60 degrees. An incision was made at the level of the cisterna magna, and skin and muscle were retracted to expose the dura mater covering the 4th ventricle. A 28-gauge needle was used to cut through the dura and allow access to the brainstem. Subsequently, a pulled glass micropipette (20-40 mm diameter tip) was used to inject AAV1-hSyn-Cre into the NTS. Stereotaxic coordinates were anterior 0.3 mm, lateral ± 0.15 mm, and ventral 0.3 mm from calamus scriptorius. The virus was injected (200 nl) by an air pressure system using picoliter air puffs through a solenoid valve (Clippard EV 24VDC) pulsed by a Grass S48 stimulator to control injection speed (40 nL/min). The pipette was removed 3 min post-injection, followed by wound closure using absorbable suture for muscle and silk suture for the skin. Subcutaneous injection of sustained-release Meloxicam (4 mg/kg) was provided as postoperative care.

Nuclei isolation
5-6 bilateral tissue dissections were placed in a dounce homogenizer with 1 mL cold (4°C) Lysis Buffer containing 10 mM trisHCl pH 8 (Sigma-Aldrich), 250 mM Sucrose (Sigma-Aldrich), 25 mM KCl, 5mM $MgCl_2$ (Sigma-Aldrich), 0.1% Triton x100 (Sigma-Aldrich), 0.5% RNasin Plus RNase Inhibitor (Promega), 0.1 mM Dithiothreitol (DTT) (Sigma-Aldrich) in UltraPure™ DNase/RNase-Free Distilled Water (Thermo Fisher Scientific). After douncing for 20 times, the solution was filtered through a sterile 20 µm Cell Strainer (pluriSelect), collected in 1.5 mL DNA LoBind® Tubes (Eppendorf), and centrifuged for 10 min at 900 g (rcf) at 4 C. The "slow sedimenting" component (debris and membranes) was aspirated and discarded while the "fast sedimenting" component (nuclear fraction) was gently resuspended in a 1 mL of Working Solution containing 1X pH 7.4 RNase free PBS (Thermo Fisher Scientific), 0.01% Albumin Bovine Serum (BSA) (Sigma-Aldrich), 0.5% RNasin Plus RNase inhibitor (Promega) in UltraPure™ DNase/RNase-Free Distilled Water (Thermo Fisher Scientific). Nuclei were kept on

ice while transferred to the BNORC Functional Genomics and Bioinformatics (FGB) Core for DroNc-seq assay.

DroNc-seq assay, library preparation, and sequencing

DroNc-seq was performed as per Habib et al., with minor modifications[30]. Briefly, nuclei stained with Hoechst 33342 (ThermoFisher, cat. R37605) were counted on a hemocytometer and diluted in NSB to ~250,000 nuclei/ml. Barcoded beads (Chemgenes, Cat # Macosko-2011-10) were size-selected using a 40 µm strainer, diluted to 350,000 per ml, and loaded onto 70 µm wide and 75 µm deep microfluidic device (Nanoshift). The nuclei and barcoded bead suspensions were loaded and run at 35 ml/hr each, along with carrier oil (BioRad Sciences, Cat # 186-4006) at 200 ul/min, to co-encapsulate single nuclei and beads in ~75 µm drops (vol. ~200 pl) at 4,500 drops/sec and double Poisson loading concentrations. The microfluidic emulsion was collected into 50 ml Falcon tubes for 10-25 min each and placed on ice 2h before droplet disruption. Individual 200µl reverse transcription (RT) reactions were performed on up to 90K beads. After further exonuclease digestion, aliquots of 800-5K beads were PCR amplified for 10 cycles, and PCR products were pooled in batches of 4 wells or 16 wells for library construction. Purified cDNA was quantified, and 550 pg of each sample was fragmented, tagged, and amplified in each Nextera reaction. Libraries were sequenced on the Illumina NextSeq500 using between 1.6–1.7 pM and 0.3 µM Read1CustSeqB (GCCTGTCCGCGGAAGCAGTGGTATCAACGCAGAGTAC) using a 20 × 8 × 60 read structure to a depth of 60,000 reads/nucleus.

DroNc-seq read alignment and gene expression quantification

Raw sequencing reads were demultiplexed to FASTQ format files using bcl2fastq (Illumina; version 2.20.0). Digital expression matrices (DGE) were generated using the Drop-Seq tools pipeline (https://github.com/broadinstitute/Drop-seq, version 2.4.0) as follows. Cell and UMI barcodes were extracted from read 1 and tagged onto read 2 --- barcodes with any base quality score <10 were filtered out. Subsequently, reads were trimmed at the 5′ end to remove any TSO sequence and at the 3′ end to remove poly(A) tails and/or (reverse complemented) barcodes and adapters. Tagged and trimmed reads were aligned with STAR (version 2.7.3) against the GRCm38 genome assembly using the GENCODE M20 primary assembly genomic annotation, pre-filtered to remove pseudogenes. Gene counts were obtained on a per-barcode basis by summarizing the unique read alignments across exons and introns, collapsing UMI barcodes at hamming distance 1.

DroNc-seq data analysis

72 DGEs (42 DGEs from the PB and 30 DGEs from the Bar dataset) were imported into RStudio (R version 3.6.3) and converted into single Seurat objects; metadata were assigned to each object before merging them[35,37,38]. Nuclei with 1) mitochondrial gene expression detection rate >10%; 2) hemoglobin gene expression detection rate >5%; 3) <250 or >2550 unique gene counts, possibly representing empty droplets or cell doublets, respectively, were removed. A post-filtered dataset of 149,159 nuclei x 28,681 genes was inputted into Seurat v3.2.3 + Harmony v1.0 pipeline[35,36,37,38]. Downstream processing was performed using functionalities available in the Seurat R package. Data were first log-normalized using *NormalizeData(),* and then *CellCycleScoring()* was used to infer G2M and S cell cycle scores. Briefly, this function classifies each cell into one of the 3 phases: G1, G2/M, and S, based on the expression of known G2/M and S phase marker genes[90]. Count data were then processed using *SCTransform()*, which performs a negative binomial-based normalization, identifies the top 3,000 variable features, and regresses out covariates. Regressed covariates included: sex, feeding schedule (fasted, re-fed, and ad libitum), CO2 treatment, mitochondrial gene detection

rate, inferred cell cycle scores, and sample ID. Principal Component Analysis (PCA) was performed on the 3,000 most variable features using the *runPCA()* function. *RunHarmony()* was subsequently used to harmonize the PB and Bar datasets' gene expression profiles. Downstream analyses were conducted on the harmonized dataset. Distinct cell clusters were determined via Shared Nearest Neighbor (SNN) and k-Nearest Neighbor (KNN) analyses. For SNN analysis, resolution parameters of 0.4 for “all nuclei” and 1 for the neurons of the “excitatory” and “inhibitory” groups were used. T-distributed stochastic neighbor embedding (t-SNE) was performed on the first 50 PCs to visualize cell clusters. Finally, DE analysis between clusters was performed using the non-parametric Wilcoxon Rank Sum test implemented in *FindAllMarkers()* and *FindMarkers()* functions. A gene was defined as differentially expressed if the absolute average log fold-change (avg_logFC) was >0.25 and the Bonferroni-adjusted p-value <0.01. Cell types were assigned to each cell cluster based on the expression of specific marker genes. Glia/non-neuronal cell types and cerebellar neurons were removed. The remaining neuronal clusters were categorized into "excitatory" and "inhibitory" (see results). Expression datasets representing “excitatory” and “inhibitory” groups were re-processed the same way as described above. Descriptive statistics relative to the abovementioned datasets are presented in SFig 1a-i.

Data analysis of the mouse PB scRNA-seq dataset from Pauli et al

scRNA-seq data were retrieved from Pauli et al. manuscript that classifies the PB neuronal types by their transcriptional profile and axonal projections[59]. 4 DGEs representing 4 experimental batches were obtained from the NCBI Gene Expression Omnibus (GEO) portal (ID GSE207708) and imported into RStudio (R version 3.6.3). A Seurat object that includes PB neurons used for graphs and as input for the *MetaNeighborUS ()* function was generated following the code available on: https://github.com/stuberlab/Pauli-Chen-Basiri-et-al-2022. DE between clusters was performed using the non-parametric Wilcoxon Rank Sum statistics implemented in *FindAllMarkers()* and *FindMarkers()* functions. A gene was defined differentially expressed if absolute logFC was >0.25 and Bonferroni-adjusted p-value <0.01.

MERFISH gene panel selection

MERFISH assay was performed by Vizgen, Inc. (Cambridge, MA, USA). (Vizgen, #10400003). A panel of 315 genes was curated to generate a custom MERSCOPE gene panel to locate both non-neuronal and neuronal clusters. Only genes that met at least one of these criteria were selected: 1- highly variable genes obtained from DE analysis of the DroNc-seq dataset (adj. p-value <0.01; Av. logFC >0.25); 2- canonical glial, non-neuronal, and neuronal markers; 3- transcriptional factors, neuropeptides, and receptors – including those which could be potential pharmacological targets. A panel of 30 encoding probes for each gene was designed by Vizgen using a proprietary algorithm, except for 11 genes where the targetable regions were <30 (STable 4). Each MERFISH encoding probe contains a targeting region complementary to the RNA of interest and a series of Vizgen's proprietary readout sequences that encode the specific barcode assigned to each RNA. In addition, 70 scrambled probes (blanks) to which have been assigned a specific binary barcode were added to the library as a negative control.

MERFISH sample preparation

A total of 7 C57BL/6J mice (4 males and 3 females) 8-10 week-old from JAX were used for the MERFISH experiment. Mice were housed and sacrificed as previously described. After decapitation, the brain was removed from the skull, chilled for 3 min in an ice-cold DMEM/F12, no phenol red (Thermo Fisher Scientific) media slush, and placed ventral surface up in an ice-cold stainless steel brain matrix (Roboz Surgical Instrument Co.). A 2 mm-thick coronal section containing the entire pons-medulla region was cut, placed in a square mold (S22, Kisker Biotech), embedded in OCT (Tissue-Tek® O.C.T. Compound, Sakura), and stored at -80°C.

Afterward, the brain block embedded in OCT was incubated for 1 hour at -20°C in a cryostat (LEICA CM1510 S CRYOSTAT), and 10 µm thick coronal sections were cut. To ensure the inclusion of our ROI, we cut from each mouse 10 sections at intervals of 80-90 µm starting approximately from -4.70 to -5.80 bregma level in the Franklin-Paxinos atlas[43]. Two sections at the time were mounted on a warm, functionalized, bead-coated MERSCOPE slide (Vizgen, #20400001) within the boundaries drawn using a 1cm^2 hexagonal gasket (Vizgen). Tissue sections were then placed face-up in a 60 mm petri dish (VWR, 25382-687) and stored at -20°C. Subsequently, 4 ml of Fixation Buffer (4% PFA; EMS, 15714) in buffered 1X PBS (ThermoFisher, AM9625) was added to each petri dish, and sections were incubated for 15 min at room T in a fume hood. After 15 minutes, the Fixation Solution was discarded, and the sections were washed 3 times, 5 minutes each, with a Washing Solution (1X PBS, ThermoFisher, AM9625) at room T. Then, 5 mL of 70% Ethanol (Sigma-Aldrich) was added to the petri dish, and sections were incubated for 5 minutes at room T. Finally, sections were transferred in a Polytube bag, 4 mm thickness (Vizgen) with 10 ml of 75% Ethanol (Sigma-Aldrich), sealed, and stored in the dark at 4°C before shipping to Vizgen facility. After washing with 5 ml Sample Preparation Wash Buffer (Vizgen, #20300001) for 5 minutes and 5 ml Formamide Wash Buffer (Vizgen, #20300002) for 30 minutes at 37°C, the sample was hybridized with the MERSCOPE Gene Panel Mix at 37°C in an incubator for 36-48 hours. The tissue slices were then washed twice with 5 ml Formamide Wash Buffer at 47°C for 30 minutes and embedded into a hydrogel using the Gel Embedding Premix (Vizgen, #20300004), ammonium persulfate (Sigma, 09913-100G), and TEMED (N,N,N',N'-tetramethylethylenediamine) (Sigma, T7024-25ML) from the MERSCOPE Sample Prep Kit (Vizgen, #0400012). After the gel embedding solution polymerized, the sample was incubated with a Clearing Solution consisting of 50 ul of Protease K (NEB, P8107S) and 5 ml of Clearing Premix (Vizgen, #20300003) at 37°C overnight. Then, the sample was washed with 5 ml Sample Preparation Wash Buffer and imaged on the MERSCOPE system (Vizgen 10000001). A fully detailed, step-by-step instruction on the MERFISH sample prep is available at: https://vizgen.com/resources/fresh-and-fixed-frozen-tissue-sample-preparation/. Full Instrumentation protocol is available at: https://vizgen.com/resources/merscope-instrument/.

MERFISH Imaging and cell segmentation

After image acquisition, the data were analyzed through the merlin pipeline through Vizgen's MERSCOPE Analysis Computer by selecting the watershed cell segmentation algorithm. Detailed documentation and the full code can be found on GitHub at: https://emanuega.github.io/MERlin/index.html# or Zenodo. at: 10.5281/zenodo.3758539 . The output files for each coronal brain section consisted of 1) **cell_by_gene.csv** - A matrix where each row corresponds to a cell and each column to a gene. The matrix is not filtered for segmentation artifacts. Before analyses, cells with <15 gene counts were removed; 2) **detected_transcripts.csv** -DataFrame of all detected transcripts in a coronal section where each row is a detected transcript. The columns are "barcode_id" – 315 internally used gene IDs that identify each gene univocally; "global_x, global_y" - the global micron x and y coordinates of each transcript; "global_z" - the index of the z-stack in the section where the transcript was detected. To note that 7 z-stacks per section were acquired at an interval of ~1.5 µm; "x, y" - the pixel coordinates of a transcript within the field of view (FOV); "fov" - the index of the FOV where the transcript was detected; "gene" - the gene name of the detected transcript; 3) **cell_metadata.csv** - Spatial metadata of detected cells. Each row corresponds to a cell. The columns are: "fov" - the field of view containing the cell; "volume" - the volume of the cell in µm^3; "center_x" - the x coordinate of the center of the cell in global micron coordinates; "center_y" - the y coordinate of the center of the cell in global micron coordinates; "min_x, max_x" - the x minimum and maximum of the bounding box containing the cell in global micron coordinates; "min_y, max_y" – the y minimum and maximum of the bounding box containing the cell in global

micron coordinates; 4) **cell_boundaries.hdf5** - Polygon boundaries relative to cells identified in a single FOV. Each file refers to a FOV. Boundaries are stored in .hdf5 format indexed by the unique cell ID; 5) **images** – Folder containing 7 mosaic_DAPI.tiff and 7 mosaic_PolyT.tiff images. These represent stitched DAPI or PolyT staining images acquired from a 10 µm thick MERFISH coronal section at ~1.5 µm intervals; micron_to_mosaic_pixel_transform.csv - contains the transformation matrix used to convert micron into pixel coordinates; manifest.json – contains the metadata of the stacked image.

MERFISH data analysis

46 mosaic DAPI images, one per coronal section, were imported into Adobe Illustrator v26.5. Using the lasso tool, the dPnTg's boundaries were manually defined for each image. The cartesian pixel coordinates defining each image's boundaries were extracted using a custom script (STable 34). Then, 46 gene count matrices (cell_by_gene.csv) related to the 46 DAPI images were imported into Python v3.7. Using the cartesian pixel coordinates defined by the lasso tool, the count matrices were subsetted to include only data relative to features (genes) and barcodes (cells) located within the defined boundaries. 46 subsetted matrices were imported into RStudio (R version 3.6.3) and converted into Seurat objects; metadata were assigned to each object before merging them[35,37,38]. Cells with <15 gene counts were filtered out. A post-filtered dataset of 685,289 cells x 315 genes was inputted into Seurat v3.2.3 + Harmony v1.0 pipeline[35,36,37,38]. Data were analyzed using the same bioinformatic pipeline employed for DroNc-seq with a few modifications. Briefly, count data were processed using *SCTransform()*. Regressed covariates included only sex. PCA was performed on the 315 features using the *runPCA()* function. Harmony was subsequently used to harmonize the gene expression profiles across the sections. Downstream analyses were conducted on the harmonized dataset. Distinct cell clusters were determined via SNN and KNN analyses. SNN analysis was based on resolution parameters of 0.4 for “all cells”, 0.8 and 0.6 for the neurons of the “excitatory” and “inhibitory” groups, respectively, 0.4 for the subregion-specific atlas_1 and 0.8 for atlases 1-3 (see results). T-SNE was used on the first 50 PCs to visualize cell clusters. Finally, DE analysis between clusters was performed using the non-parametric Wilcoxon Rank Sum statistics implemented in *FindAllMarkers()* and *FindMarkers()* functions. A gene was defined as differentially expressed if the absolute average log fold-change (avg_logFC) was >0.25 and the Bonferroni-adjusted p-value <0.01. As in DroNc-seq analysis, after assigning all the clusters to a cell type, clusters corresponding to glial/non-neuronal cell types and cerebellar neurons were discarded. The remaining neuronal clusters were divided into "excitatory" and "inhibitory". They underwent the same analyses as described above. Descriptive statistics relative to the abovementioned datasets are in SFig 6a-h. Next, raw and normalized gene count matrices, metadata, and cartesian pixel coordinates of each polygon were extracted from the three Seurat objects containing “all cells”, “excitatory”, and “inhibitory” neurons and imported into GIOTTO v1.1.2 package for data visualization[91]. The function *createGiottoObject()* was used to create a single GIOTTO object representing the cells of the dPnTg across 46 sections and *subsetGiottoLocs()* to subset the gene count matrices based on spatial coordinates to generate the 4 anatomical subregions that were then analyzed using Seurat v3.2.3 + Harmony v1.0 pipeline described above.

Estimation of clusters’ replicability

The R package MetaNeighbor version 1.14.0[44,45] was employed to assess cluster replicability across technologies (i.e., MERFISH, DroNc-seq, snRNA-seq(10X), scRNA-seq (10X)) and species (i.e., homo sapiens, mus musculus). Four main comparisons were made using MetaNeighbor: 1) across technologies, between MERFISH and DroNc-seq neuronal datasets of the mouse dPnTg and 2) between MERFISH and scRNA-seq neuronal datasets of the mouse PB; 3) across species, between the mouse and human neuronal datasets of the dPnTg; and 4)

between the mouse DroNc-seq "excitatory" (after excluding non-PB clusters 9-10, 15, 19-20, 25-26, 30, 32) and the human snRNA-seq neuronal datasets of the PB (after excluding GABAergic clusters). For the cross-species analyses (points 2 and 3), gene symbols were converted between species using a manifest file ("gene_orthologs.gz") listing gene symbol correspondences across species as available at NCBI (https://ftp.ncbi.nlm.nih.gov/gene/DATA/). Briefly, unique IDs were assigned to neuronal clusters of the two datasets. Next, metadata were assigned to each dataset, and both Seurat objects were converted into SingleCellExperiment objects using the function *as.SingleCellExperiment().* The two objects were then merged using the *mergeSCE()* function from the MetaNeighbor package. The function selects only genes, assays, and metadata columns shared by the two objects. The function *variableGenes()* was used to select genes with high variance in both datasets. In the comparison between MERFISH and DroNc-seq (point 1), the 315-panel genes were set as highly variable genes.
The unsupervised *MetaNeighborUS()* function with the "fast_version" parameter set to TRUE was used to assess cell type homology. The *topHits()* function was used to select only matches with an AUROC >0.80 (MERFISH vs DroNc-seq), >0.85 (MERFISH vs scRNA-seq (Pauli et al.[59]), and mouse vs human (Siletti et al.[83]) and/ or classified as "reciprocal" top hits.

Functional classification of gene sets driving cell type replicability
In cross-species analysis (as per point 3 in the above paragraph), we conducted gene ontology (GO) enrichment analysis of the gene sets driving the cluster replicability. A list of GO sets (*Mus Musculus*) comprising 22,546 GO terms categorized into the 3 main categories, Cellular Component (CC), Molecular Function (MF), and Biological Process (BP), was downloaded from https://figshare.com/articles/dataset/Protocol_data_R_version_/13020569/2[45]. The GO sets were filtered to (i) only include genes shared with our merged human-mouse dataset and (ii) be large enough to learn expression profiles (>10 genes) and small enough to enrich for GO terms (<100), following published works[45]. Finally, the supervised *MetaNeighbor()* function was employed to construct a rank correlation network between cells for a gene set and predict cell type membership. The resulting AUROC, in this case, represents how well cells can be assigned to a cell type label using individual GO gene sets (how well a gene set contributes to each cell-type replicability). AUROC values of ~0.5–0.6 indicate random performance, AUROC values of ~0.7 indicates that they contribute moderately to replicability, while AUROC values >0.8 indicate high performance[45].

Correspondence between cells from DroNc-seq and MERFISH datasets used in the spatial dashboard
To find a correspondence between cells from DroNc-seq and MERFISH clusters, we applied the following functions built-in Seurat v3.2.3: 1) *FindTransferAnchors()*, which performs a CCA on the reference (DroNc-seq) and query (MERFISH) and identify cell anchors which are used to transfer data from the reference to the query; 2)*TransferData()* to transfer labels across single-cell datasets. The function's output includes a *prediction score* for each MERFISH cell in a DroNc-seq cluster and a *max prediction score* with the respective *predicted id*, i.e., the predicted DroNc-seq cluster for each MERFISH cell ID that has the highest score.

Specificity, sensitivity, and reproducibility of MERFISH assay
MERFISH efficiency was evaluated by measuring the number of transcripts per FOV (FOV size = 200 x 200 µm). Only slices with >25,000 transcript counts per FOV were retained (SFig 3a). As a control for MERFISH specificity, for all the sections was demonstrated 1) a Pearson's *r* correlation coefficient >70% with a bulk RNA-seq dataset from the whole mouse brain (SFig 3b, 2f; STable 35) and 2) a difference of 15.3 folds from the non-specific signal (SFig 5a). For the MERFISH dataset, the average expression of the 315 genes was calculated across all cells and is reported as log10 raw counts (or log10 (raw counts+1)). For the bulk RNA-seq dataset, the

average expression of the 315 genes was calculated across all samples and is reported as log10 FPKM (Fragments per kilobase of transcript per million mapped fragments). Pearson's *r* correlation between the average expression values of the 315 genes in MERFISH and bulk RNA-seq datasets was performed by matching the same isoform between the two sources (see codebook STable 36). The bulk RNA-seq dataset from the whole mouse brain can be retrieved at https://www.ebi.ac.uk/arrayexpress/experiments/E-MTAB-6081/.
Experimental reproducibility was evaluated by computing the Pearson's *r* correlation coefficient of the average gene expression of 315 genes between sections of the same mouse (intra-batch reproducibility) and sections of different mice (inter-batch reproducibility) (SFig 4a-b). Sequential sections exhibited a higher pairwise correlation compared to non-sequential sections. (SFig 4a-a, 5c) In addition, the correlations between two coronal sections from the same or two different mice, representing approximately the same bregma level, were always extremely high (r>0.99, p=0) (SFig 5d-e).
The difference in sensitivity between MERFISH and DroNc-seq was estimated by computing the fold change between the average expression levels of 315 genes across all cells in DroNc-seq versus MERFISH datasets. Average gene expression was 13.2 folds higher in MERFISH compared to the DroNc-seq dataset (SFig 5b); this evidence was in line with a difference of 6.4 folds between MERFISH and scRNA-seq reported by Moffit et al.[31] In addition, the DroNc-seq DGE matrix was sparser (0.96% of zeros) than the MERFISH gene count matrix (0.81% of zeros), as previously reported[86]. This could align with the observation of a lower Spearman's *rho* correlation between MERFISH versus DroNc-seq *(p*=58) compared to MERFISH versus bulk RNA-seq (*p*=69). Spearman's *rho* correlation was lower in the first correlation, despite both techniques sampled only the dPnTg, while bulk RNA-seq referred to the whole mouse brain (SFig 2f-g).

Interactive visualization of MERFISH and DroNc-seq data
The design and realization of a dashboard able to produce interactive visualization of spatial-transcriptomic data were done in partnership with HEAVY.AI. The dashboard hosts 2 viewers on 2 different pages: the first viewer, called “spatial cell viewer,” displays a total of 14 full, 10 µm thick coronal sections and covers at an interval of 80-90 µm a region from -4.7 to -5.8 bregma level in the Franklin-Paxinos atlas[43], whereas the second viewer, called “subregion cell viewer”, hosts the data relative to the 4 subsetted regions (see section “ MERFISH data analysis”). The dashboard can be accessed at: http://harvard.heavy.ai:6273/. Full documentation can be found at: https://docs.heavy.ai/?_ga=2.207206352.2137306788.1595867219-1426127794.1594677732. Transcriptomic data for each of the 3 DroNc-seq and 7 MERFISH datasets, all the raw and normalized count matrices, the cell metadata, and the t-SNE embeddings were uploaded on the single-cell BROAD portal. The study can be accessed at: https://singlecell.broadinstitute.org/single_cell/study/SCP1808. Full documentation can be found at: https://singlecell.zendesk.com/hc/en-us.

Data analysis of the human brain snRNA-seq dataset
snRNA-seq data were retrieved from a preprint by Siletti et al., describing the transcriptome of the entire adult human brain at a single-nucleus resolution[83]. A single .loom file containing a prefiltered DGE (for low-quality nuclei/ doublets) of over 3 million nuclei and relative metadata was imported into Python v3.7. The .loom object was subsetted to include only nuclei belonging to anatomical dissections of 1) the pontine reticular formation (PnRF) and the PB or 2) other nuclei in the dPnTg and the DTg. A subsetted .loom object of 24,977 nuclei x 35,003 genes was then imported into R and processed using the Seurat v3.2.3 + Harmony v1.0 pipeline[36,37,38,39]. *As.Seurat()* was employed to convert the .loom file into a Seurat object. Data were analyzed using the same bioinformatic pipeline employed for DroNc-seq and MERFISH with a few modifications. Briefly, count data were processed using *SCTransform()*. Regressed covariates

included: age, cell cycle score, 10X chemistry, mitochondrial gene detection rate, donor label, and anatomical dissection. The data were derived from 3 male donors. PCA was performed on the 3,000 most variable features. *RunHarmony()* was subsequently used to harmonize the gene expression across different donors. Distinct cell clusters were determined via SNN and KNN analyses in Seurat. SNN analysis was based on resolution parameters of 0.4 for “all nuclei”, 0.8 for the neurons of the “excitatory” and inhibitory “groups”, and 0.6 for all PB neurons. t-SNE was used on the first 50 PCs to visualize cell clusters. DE analysis between clusters was performed using the non-parametric Wilcoxon Rank Sum statistics implemented in *FindAllMarkers()* and *FindMarkers()* functions. A gene was defined as differentially expressed if the absolute average log fold-change (avg_logFC) was >0.25 and the Bonferroni-adjusted p-value <0.01. Consistently with MERFISH and DroNc-seq analyses, all the clusters were assigned to a cell type. Clusters corresponding to glia/ non-neuronal cell types and cerebellar neurons were discarded. The remaining neuronal clusters were divided into "excitatory" and "inhibitory". They underwent the same analyses as described above. The whole DGE and relative cell metadata are stored as .loom files and are available for download at https://storage.cloud.google.com/linnarsson-lab-human[83].

RNA scope in situ hybridization

RNA Scope Multiplex Fluorescent Reagent Kit V2 (Advanced Cell Diagnostics, Hayward, CA; Cat. #323100) was used to perform RNA scope in situ hybridization for *Pdyn*, *Gpr101*, and *Foxp2* mRNA. Mice were, first, intracardially perfused with formalin (10% buffered solution) under deep anesthesia induced by isoflurane exposure (5% in O2), and then brains were removed from the skull and post-fixed in formalin (10% buffered solution) overnight. After incubating in 20% sucrose (for cryoprotection) for 24 h, the brains were cut into 30 µm-thick sections. Sections were treated with protease (40˚C; 30min; Protease IV, RNA scope) and incubated with RNA scope probes for *Pdyn*-C1 (RNA scope® Probe- Mm-Pdyn; Cat. #318771), *Gpr101*-C2 (RNA scope® Probe- Mm-*Gpr101*; Cat. #317281), and *Foxp2*-C3 (RNA scope® Probe-Mm-Foxp2; Cat. #428791; Advanced Cell Diagnostics) during the hybridization step (2 h; 40°C). After the hybridization step, we performed three amplification steps (40°C; AMP1-FL and AMP2-FL: 30 min each; AMP3-FL: 15 min), followed by horse radish peroxidase-C1 (HRP-C1) amplification (40°C for 15 min). Sections were then incubated in TSA plus Fluorescein (Perkin Elmer, Cat. #NEL744001KT) to visualize *Pdyn* mRNA (Channel 1 at 488nm) in green. This is followed by incubating the sections in HRP-C2 amplification step (40°C; 15 min). Sections were then incubated in TSA plus Cy3 (Perkin Elmer, Cat. #: NEL754001KT) fluorophore (1:1000; 30 min) to visualize *Gpr101* mRNA (Channel 2 at 550 nm) in red. In the last step of the process, sections were subjected to HRP-C3 amplification (40°C; 15 min) followed by TSA plus Cy5 incubation (40°C; 30 min; Perkin Elmer; Cat. #NEL754001KT) to visualize *Foxp2* mRNA (Channel 3 at 647 nm) in magenta. After each fluorophore step, sections were subjected to HRP blocking (40°C; 15 min). After each step in the protocol, the sections were washed two times with 1X wash buffer provided in the kit. The covered sections (Vectashield mounting medium; Vector Laboratories) were imaged and photographed with a confocal microscope (Leica Stellaris 5) at final magnification of 20X and 63X.

Graphics

All graphic representations were generated using R (version 3.6.3) base functions or R packages. Bar plots, scatter plots, box plots, donut plots, staked area charts, line charts, and correlation matrix heatmaps were generated with R base functions or the ggplot2 package[92]. Sankey plots were generated with the networkD3 package. Dot plots, t-SNEs, and violin plots were generated using functions built in the Seurat v3.2.3 package[38]. Voronoi plots were generated using the functions built in the GIOTTO v1.1.2 package[91]. Human-mouse dot plots were generated using the function built in the MetaNeighbor package[44,45].

Statistics and reproducibility
No statistical method was used to predetermine the sample size. Our sample sizes for MERFISH and DroNc-seq are similar to or bigger than those reported in the literature[46,93,47]. No randomization or blinding was performed for sample collection and data analysis. This was unrequired since we did not perform any comparison between different conditions or treatments. The criteria used to exclude data during the quality control process for MERFISH, DroNc-seq, and human snRNA-seq are documented in the "MERFISH data analysis", "DroNc-seq data analysis", and "Data analysis of the human brain snRNA-seq dataset" sections, respectively.

Acknowledgments
We thank Dr. Jiang He and Dr. George Emanuel from Vizgen for consenting us to enroll in the Vizgen early access program and granting us access to MERSCOPE before commercialization. We thank Mr. Tony Duarte from HEAVY.AI for his availability and collaboration in implementing our vision to use their HEAVY.AI proprietary GPU-accelerated technology to query single-cell spatial transcriptomic datasets in real-time. This project was funded by the NIH grants R01DK075632 (B.B.L), P01HL149630, NS072337 (C.B.S), R01-DK125708 (A.M.J.V.), R01-DK113030, P20-DK119789 (M.L.Z.), R01-NS091126 (E.A.), R00HL144923 (J.M.R), DP1-AT010971, R01-MH12343 (M.L.A.).

Author contributions
Project design: B.B.L., S.N. A.M.J.V. Project management: B.B.L., S.N., A.M.J.V, R.D.L. Data generation (DroNc-seq): S.N., A.M.J.V., N.K., R.D.L., J.M.R., D.P., M.V. Data generation (MERFISH): S.N., R.D.L., N.K. Data processing (DroNc-seq): C.L.J, H.S. Data processing (MERFISH): S.N., Data analysis (DroNc-seq): S.N., A.Z. Data analysis (MERFISH): S.N., A.Z. Data storage (DroNc-seq/ MERFISH): O.A., S.N. Spatial dashboard design: S.N., D.N., C.B. Animal experiments: A.M.J.V., N.K., Z.Y., R.M.G, S.N, R.D.L. In situ hybridization: R.D.L. Anatomic cluster annotation: S.N., R.D.L., C.B.S., A.M.J.V., N.K. Drafting of the manuscript and figure generation: S.N., R.D.L., E.A, A.M.J.V., N.K. Manuscript review and editing: S.N., B.B.L, A.M.J.V., C.B.S., A.Z., R.D.L., E.A., M.L.A., L.T., K.D.H., M.L.Z. Vizgen team contributed to MERFISH data generation and data processing. HEAVY.AI team contributed to the spatial design and implementation of the spatial viewer.

Data availability
Mouse DroNc-seq raw and processed data from this study are accessible from the GEO portal under the accession number GSE226809. Mouse MERFISH raw and processed data from this study are under the BIDMC repository:
https://research.bidmc.harvard.edu/datashare/DataShareInfo.ASP?Submit=Display&ID=7.
Mouse PB raw and processed data from Pauli et al. are accessible from the GEO portal under the accession number GSE207708. Human snRNA-seq processed data from Siletti et al. are deposited in a bucket on Google Cloud under the following link:
https://storage.cloud.google.com/linnarsson-lab-human.

Code availability
Python and R codes used in the manuscript are available upon request.

Conflict of Interest
Cory Brannigan is a software architect at HEAVY.AI.

REFERENCES

1. Miller, J. R. *et al.* A Subregion of the Parabrachial Nucleus Partially Mediates Respiratory Rate Depression from Intravenous Remifentanil in Young and Adult Rabbits. *Anesthesiology* **127**, 502–514 (2017).
2. Kaur, S. & Saper, C. B. Neural Circuitry Underlying Waking Up to Hypercapnia. *Front. Neurosci.* **13**, 401 (2019).
3. Poe, G. R. *et al.* Locus coeruleus: a new look at the blue spot. *Nat. Rev. Neurosci.* **21**, 644–659 (2020).
4. Breton-Provencher, V., Drummond, G. T. & Sur, M. Locus Coeruleus Norepinephrine in Learned Behavior: Anatomical Modularity and Spatiotemporal Integration in Targets. *Front. Neural Circuits* **15**, 638007 (2021).
5. Ryan, P. J., Ma, S., Olucha-Bordonau, F. E. & Gundlach, A. L. Nucleus incertus—An emerging modulatory role in arousal, stress and memory. *Neurosci. Biobehav. Rev.* **35**, 1326–1341 (2011).
6. Ma, S. & Gundlach, A. L. Ascending Control of Arousal and Motivation: Role of Nucleus Incertus and its Peptide Neuromodulators in Behavioural Responses to Stress. *J. Neuroendocrinol.* **27**, 457–467 (2015).
7. Lu, L. *et al.* Control of locomotor speed, arousal, and hippocampal theta rhythms by the nucleus incertus. *Nat. Commun.* **11**, 262 (2020).
8. Scammell, T. E., Arrigoni, E. & Lipton, J. O. Neural Circuitry of Wakefulness and Sleep. *Neuron* **93**, 747–765 (2017).
9. Deng, J. *et al.* The Parabrachial Nucleus Directly Channels Spinal Nociceptive Signals to the Intralaminar Thalamic Nuclei, but Not the Amygdala. *Neuron* **107**, 909-923.e6 (2020).

10. Barik, A. *et al.* A spinoparabrachial circuit defined by Tacr1 expression drives pain. *eLife* **10**, e61135 (2021).

11. Coimbra, B. *et al.* Role of laterodorsal tegmentum projections to nucleus accumbens in reward-related behaviors. *Nat. Commun.* **10**, 4138 (2019).

12. Hernandez, N. S. *et al.* GLP-1 receptor signaling in the laterodorsal tegmental nucleus attenuates cocaine seeking by activating GABAergic circuits that project to the VTA. *Mol. Psychiatry* **26**, 4394–4408 (2021).

13. Liu, Z. *et al.* Dorsal Raphe Neurons Signal Reward through 5-HT and Glutamate. *Neuron* **81**, 1360–1374 (2014).

14. Taube, J. S. The Head Direction Signal: Origins and Sensory-Motor Integration. *Annu. Rev. Neurosci.* **30**, 181–207 (2007).

15. Florez-Paz, D., Bali, K. K., Kuner, R. & Gomis, A. A critical role for Piezo2 channels in the mechanotransduction of mouse proprioceptive neurons. *Sci. Rep.* **6**, 25923 (2016).

16. Szőnyi, A. *et al.* Brainstem nucleus incertus controls contextual memory formation. *Science* **364**, eaaw0445 (2019).

17. Bassant, M.-H. & Poindessous-Jazat, F. Ventral tegmental nucleus of Gudden: A pontine hippocampal theta generator? *Hippocampus* **11**, 809–813 (2001).

18. Sciolino, N. R. *et al.* Natural locus coeruleus dynamics during feeding. *Sci. Adv.* **8**, eabn9134.

19. Lowell, B. B. New Neuroscience of Homeostasis and Drives for Food, Water, and Salt. *N. Engl. J. Med.* **380**, 459–471 (2019).

20. Li, M. M. *et al.* The Paraventricular Hypothalamus Regulates Satiety and Prevents Obesity via Two Genetically Distinct Circuits. *Neuron* **102**, 653-667.e6 (2019).

21. Kim, D.-Y. *et al.* A neural circuit mechanism for mechanosensory feedback control of ingestion. *Nature* **580**, 376–380 (2020).

22. Barrington, F. THE EFFECT OF LESIONS OF THE HIND□ AND MID□BRAIN ON MICTURITION IN THE CAT. *Exp. Physiol.* **15**, 81–102.

23. Fowler, C. J., Griffiths, D. & de Groat, W. C. The neural control of micturition. *Nat. Rev. Neurosci.* **9**, 453–466 (2008).

24. Verstegen, A. M. J., Vanderhorst, V., Gray, P. A., Zeidel, M. L. & Geerling, J. C. Barrington's nucleus: Neuroanatomic landscape of the mouse "pontine micturition center": VERSTEGEN et al. *J. Comp. Neurol.* **525**, 2287–2309 (2017).

25. Campos, C. A., Bowen, A. J., Roman, C. W. & Palmiter, R. D. Encoding of danger by parabrachial CGRP neurons. *Nature* **555**, 617–622 (2018).

26. Geerling, J. C. *et al.* Genetic identity of thermosensory relay neurons in the lateral parabrachial nucleus. *Am. J. Physiol.-Regul. Integr. Comp. Physiol.* **310**, R41–R54 (2016).

27. Norris, A. J., Shaker, J. R., Cone, A. L., Ndiokho, I. B. & Bruchas, M. R. Parabrachial opioidergic projections to preoptic hypothalamus mediate behavioral and physiological thermal defenses. *eLife* **10**, e60779 (2021).

28. Davern, P. J. A role for the lateral parabrachial nucleus in cardiovascular function and fluid homeostasis. *Front. Physiol.* **5**, (2014).

29. Piyush Shah, D. & Barik, A. The Spino-Parabrachial Pathway for Itch. *Front. Neural Circuits* **16**, 805831 (2022).

30. Habib, N. *et al.* Massively parallel single-nucleus RNA-seq with DroNc-seq. *Nat. Methods* **14**, 955–958 (2017).

31. Moffitt, J. R. *et al.* Molecular, spatial, and functional single-cell profiling of the hypothalamic preoptic region. *Science* **362**, eaau5324 (2018).

32. Bakken, T. E. *et al.* Single-nucleus and single-cell transcriptomes compared in matched cortical cell types. *PLOS ONE* **13**, e0209648 (2018).

33. Lake, B. B. *et al.* A comparative strategy for single-nucleus and single-cell transcriptomes confirms accuracy in predicted cell-type expression from nuclear RNA. *Sci. Rep.* **7**, 6031 (2017).

34. Ding, J. *et al.* Systematic comparison of single-cell and single-nucleus RNA-sequencing methods. *Nat. Biotechnol.* **38**, 737–746 (2020).

35. Butler, A., Hoffman, P., Smibert, P., Papalexi, E. & Satija, R. Integrating single-cell transcriptomic data across different conditions, technologies, and species. *Nat. Biotechnol.* **36**, 411–420 (2018).

36. Korsunsky, I. *et al.* Fast, sensitive and accurate integration of single-cell data with Harmony. *Nat. Methods* **16**, 1289–1296 (2019).

37. Hafemeister, C. & Satija, R. Normalization and variance stabilization of single-cell RNA-seq data using regularized negative binomial regression. *Genome Biol.* **20**, 296 (2019).

38. Stuart, T. *et al.* Comprehensive Integration of Single-Cell Data. *Cell* **177**, 1888-1902.e21 (2019).

39. Kozareva, V. *et al.* A transcriptomic atlas of mouse cerebellar cortex comprehensively defines cell types. *Nature* **598**, 214–219 (2021).

40. Rosenberg, A. B. *et al.* Single-cell profiling of the developing mouse brain and spinal cord with split-pool barcoding. *Science* **360**, 176–182 (2018).

41. Root, D. H. *et al.* Single rodent mesohabenular axons release glutamate and GABA. *Nat. Neurosci.* **17**, 1543–1551 (2014).

42. Huang, D. *et al.* Neuropeptide S (NPS) neurons: Parabrachial identity and novel distributions. *J. Comp. Neurol.* **n/a**, (2022).

43. Paxinos, G. & Franklin, K. B. J. The Mouse Brain in Stereotaxic Coordinates.

44. Crow, M., Paul, A., Ballouz, S., Huang, Z. J. & Gillis, J. Characterizing the replicability of cell types defined by single cell RNA-sequencing data using MetaNeighbor. *Nat. Commun.* **9**, 884 (2018).

45. Fischer, S., Crow, M., Harris, B. D. & Gillis, J. Scaling up reproducible research for single-cell transcriptomics using MetaNeighbor. *Nat. Protoc.* **16**, 4031–4067 (2021).

46. Moffitt, J. R. *et al.* Molecular, spatial, and functional single-cell profiling of the hypothalamic preoptic region. *Science* **362**, eaau5324 (2018).

47. Chen, R. *et al.* Decoding molecular and cellular heterogeneity of mouse nucleus accumbens. *Nat. Neurosci.* **24**, 1757–1771 (2021).

48. Olszewski, J. & Baxter, D. Cytoarchitecture of the human brainstem. By Jerzy Olszewski and Donald Baxter. Published and distributed in North America for S. Karger by J. B. Lippincott Company, Philadelphia and Montreal. 1954. 199 pages. Price $16.00 (Reviewed by Gerhardt von Bonin). *J. Comp. Neurol.* **101**, 825–825 (1954).

49. Varga, A. G., Maletz, S. N., Bateman, J. T., Reid, B. T. & Levitt, E. S. Neurochemistry of the Kölliker-Fuse nucleus from a respiratory perspective. *J. Neurochem.* **156**, 16–37 (2021).

50. Fulwiler, C. E. & Saper, C. B. Subnuclear organization of the efferent connections of the parabrachial nucleus in the rat. *Brain Res. Rev.* **7**, 229–259 (1984).

51. Kaur, S. *et al.* A Genetically Defined Circuit for Arousal from Sleep during Hypercapnia. *Neuron* **96**, 1153-1167.e5 (2017).

52. Kaur, S. *et al.* Role of serotonergic dorsal raphe neurons in hypercapnia-induced arousals. *Nat. Commun.* **11**, 2769 (2020).

53. Huang, D., Grady, F. S., Peltekian, L., Laing, J. J. & Geerling, J. C. Efferent projections of CGRP/Calca-expressing parabrachial neurons in mice. *J. Comp. Neurol.* **529**, 2911–2957 (2021).

54. Geerling, J. C., Yokota, S., Rukhadze, I., Roe, D. & Chamberlin, N. L. Kölliker-Fuse GABAergic and glutamatergic neurons project to distinct targets: GEERLING et al. *J. Comp. Neurol.* **525**, 1844–1860 (2017).

55. Jarvie, B. C., Chen, J. Y., King, H. O. & Palmiter, R. D. Satb2 neurons in the parabrachial nucleus mediate taste perception. *Nat. Commun.* **12**, 224 (2021).

56. Garfield, A. S. *et al.* A Parabrachial-Hypothalamic Cholecystokinin Neurocircuit Controls Counterregulatory Responses to Hypoglycemia. *Cell Metab.* **20**, 1030–1037 (2014).

57. Ryan, P. J., Ross, S. I., Campos, C. A., Derkach, V. A. & Palmiter, R. D. Oxytocin-receptor-expressing neurons in the parabrachial nucleus regulate fluid intake. *Nat. Neurosci.* **20**, 1722–1733 (2017).

58. Kaur, S. & Saper, C. FoxP2 cells in the lateral parabrachial area may drive respiratory responses to hypercapnia. *FASEB J.* **35**, (2021).

59. Pauli, J. L. *et al.* Molecular and anatomical characterization of parabrachial neurons and their axonal projections. *eLife* **11**, e81868 (2022).

60. Lazarov, N. E. Neurobiology of orofacial proprioception. *Brain Res. Rev.* **56**, 362–383 (2007).

61. Guyenet, P. G. The coeruleospinal noradrenergic neurons: Anatomical and electrophysiological studies in the rat. *Brain Res.* **189**, 121–133 (1980).

62. Loughlin, S. E., Foote, S. L. & Fallon, J. H. Locus coeruleus projections to cortex: Topography, morphology and collateralization. *Brain Res. Bull.* **9**, 287–294 (1982).

63. Gasparini, S., Resch, J. M., Gore, A. M., Peltekian, L. & Geerling, J. C. Pre-locus coeruleus neurons in rat and mouse. *Am. J. Physiol.-Regul. Integr. Comp. Physiol.* **320**, R342–R361 (2021).

64. Geerling, J. C. & Loewy, A. D. Aldosterone-sensitive neurons in the nucleus of the solitary tract: Efferent projections. *J. Comp. Neurol.* **497**, 223–250 (2006).

65. Jarvie, B. C. & Palmiter, R. D. HSD2 neurons in the hindbrain drive sodium appetite. *Nat. Neurosci.* **20**, 167–169 (2017).

66. Gasparini, S. *et al.* Aldosterone-sensitive HSD2 neurons in mice. *Brain Struct. Funct.* **224**, 387–417 (2019).

67. Geerling, J. C. *et al.* FoxP2 expression defines dorsolateral pontine neurons activated by sodium deprivation. *Brain Res.* **1375**, 19–27 (2011).

68. Huang, D., Grady, F. S., Peltekian, L. & Geerling, J. C. Efferent projections of Vglut2, Foxp2, and Pdyn parabrachial neurons in mice. *J. Comp. Neurol.* **529**, 657–693 (2021).

69. McKinley, M. J. *et al.* The median preoptic nucleus: front and centre for the regulation of body fluid, sodium, temperature, sleep and cardiovascular homeostasis. *Acta Physiol.* **214**, 8–32 (2015).

70. Sakakibara, R. Chapter 15 - Lower urinary tract dysfunction in patients with brain lesions. in *Handbook of Clinical Neurology* (eds. Vodušek, D. B. & Boller, F.) vol. 130 269–287 (Elsevier, 2015).

71. Sugaya, K., Matsuyama, K., Takakusaki, K. & Mori, S. Electrical and chemical stimulations of the pontine micturition center. *Neurosci. Lett.* **80**, 197–201 (1987).

72. Loewy, A. D., Saper, C. B. & Baker, R. P. Descending projections from the pontine micturition center. *Brain Res.* **172**, 533–538 (1979).

73. Valentino, R. J., Pavcovich, L. A. & Hirata, H. Evidence for corticotropin-releasing hormone projections from Barrington's nucleus to the periaqueductal gray and dorsal motor nucleus of the vagus in the rat. *J. Comp. Neurol.* **363**, 402–422 (1995).

74. Keller, J. A. *et al.* Voluntary urination control by brainstem neurons that relax the urethral sphincter. *Nat. Neurosci.* **21**, 1229–1238 (2018).

75. Mallory, B. S., Roppolo, J. R. & de Groat, W. C. Pharmacological modulation of the pontine micturition center. *Brain Res.* **546**, 310–320 (1991).

76. Kawatani, M. *et al.* Cholinergic modulation of CRH and non-CRH neurons in Barrington's nucleus of the mouse. *J. Neurophysiol.* **124**, 443–457 (2020).

77. Paxinos, G., Xu-Feng, H., Sengul, G. & Watson, C. Chapter 8 - Organization of Brainstem Nuclei. in *The Human Nervous System (Third Edition)* (eds. Mai, J. K. & Paxinos, G.) 260–327 (Academic Press, 2012). doi:10.1016/B978-0-12-374236-0.10008-2.

78. Luquin, E., Huerta, I., Aymerich, M. S. & Mengual, E. Stereological Estimates of Glutamatergic, GABAergic, and Cholinergic Neurons in the Pedunculopontine and Laterodorsal Tegmental Nuclei in the Rat. *Front. Neuroanat.* **12**, 34 (2018).

79. Boucetta, S., Cissé, Y., Mainville, L., Morales, M. & Jones, B. E. Discharge Profiles across the Sleep–Waking Cycle of Identified Cholinergic, GABAergic, and Glutamatergic Neurons in the Pontomesencephalic Tegmentum of the Rat. *J. Neurosci.* **34**, 4708–4727 (2014).

80. Lu, J., Sherman, D., Devor, M. & Saper, C. B. A putative flip–flop switch for control of REM sleep. *Nature* **441**, 589–594 (2006).

81. Hernandez, N. S. *et al.* GLP-1 receptor signaling in the laterodorsal tegmental nucleus attenuates cocaine seeking by activating GABAergic circuits that project to the VTA. *Mol. Psychiatry* **26**, 4394–4408 (2021).

82. Dillingham, C. M. *et al.* Calcium-binding protein immunoreactivity in Gudden's tegmental nuclei and the hippocampal formation: differential co-localization in neurons projecting to the mammillary bodies. *Front. Neuroanat.* **9**, (2015).

83. Siletti, K. *et al. Transcriptomic diversity of cell types across the adult human brain*. http://biorxiv.org/lookup/doi/10.1101/2022.10.12.511898 (2022) doi:10.1101/2022.10.12.511898.

84. de Lacalle, S. & Saper, C. B. Calcitonin gene-related peptide-like immunoreactivity marks putative visceral sensory pathways in human brain. *Neuroscience* **100**, 115–130 (2000).

85. Adori, C. *et al.* Neuropeptide S- and Neuropeptide S receptor-expressing neuron populations in the human pons. *Front. Neuroanat.* **9**, (2015).

86. Liu, J. *et al.* Concordance of MERFISH spatial transcriptomics with bulk and single-cell RNA sequencing. *Life Sci. Alliance* **6**, e202201701 (2023).

87. Luo, L., Callaway, E. M. & Svoboda, K. Genetic Dissection of Neural Circuits: A Decade of Progress. *Neuron* **98**, 256–281 (2018).

88. Daigle, T. L. *et al.* A Suite of Transgenic Driver and Reporter Mouse Lines with Enhanced Brain-Cell-Type Targeting and Functionality. *Cell* **174**, 465-480.e22 (2018).

89. Roman, C. W., Derkach, V. A. & Palmiter, R. D. Genetically and functionally defined NTS to PBN brain circuits mediating anorexia. *Nat. Commun.* **7**, 11905 (2016).

90. Kowalczyk, M. S. *et al.* Single-cell RNA-seq reveals changes in cell cycle and differentiation programs upon aging of hematopoietic stem cells. *Genome Res.* **25**, 1860–1872 (2015).

91. Dries, R. *et al*. Giotto: a toolbox for integrative analysis and visualization of spatial expression data. *Genome Biol.* **22**, 78 (2021).

92. Wickham, H. *ggplot2*. (Springer New York, 2009). doi:10.1007/978-0-387-98141-3.

93. Zhang, M. *et al.* Spatially resolved cell atlas of the mouse primary motor cortex by MERFISH. *Nature* **598**, 137–143 (2021).

abbreviation	brain nucleus
Bar	Barrington's nucleus
CGA	central gray, alpha part
CGB	central gray, beta part
CGPn	central gray of the pons
DR	dorsal raphe nucleus
DTgC	dorsal tegmental nucleus, central part
DTgP	dorsal tegmental nucleus, pericentral part
KF	Kölliker-Fuse nucleus
LC	locus coeruleus
LDTg	laterodorsal tegmental nucleus
LDTgV	laterodorsal tegmental nucleus, ventral
LPB	lateral parabrachial nucleus
LPBC	LPB, central part
LPBCr	LPB, crescent part
LPBD	LPB, dorsal part
LPBE	LPB, external part
LPBI	LPB, internal part
LPBS	LPB, superior part
LPBV	LPB, ventral part
Me5 or MTN	mesencephalic trigeminal nucleus
MnR	median raphe nucleus
MPB	medial parabrachial nucleus
MPBE	MPB, external part
O or NI	nucleus O or nucleus incertus
PB	parabrachial nucleus
PBW	parabrachial nucleus, waist part
PDTg	posterodorsal tegmental nucleus
PPTg	pedunculopontine tegmental nucleus
pre-LC	pre locus coeruleus
Sph	sphenoid nucleus
SPTg	subpedencular tegmental nucleus
VTg	ventral tegmental nucleus

Table 1

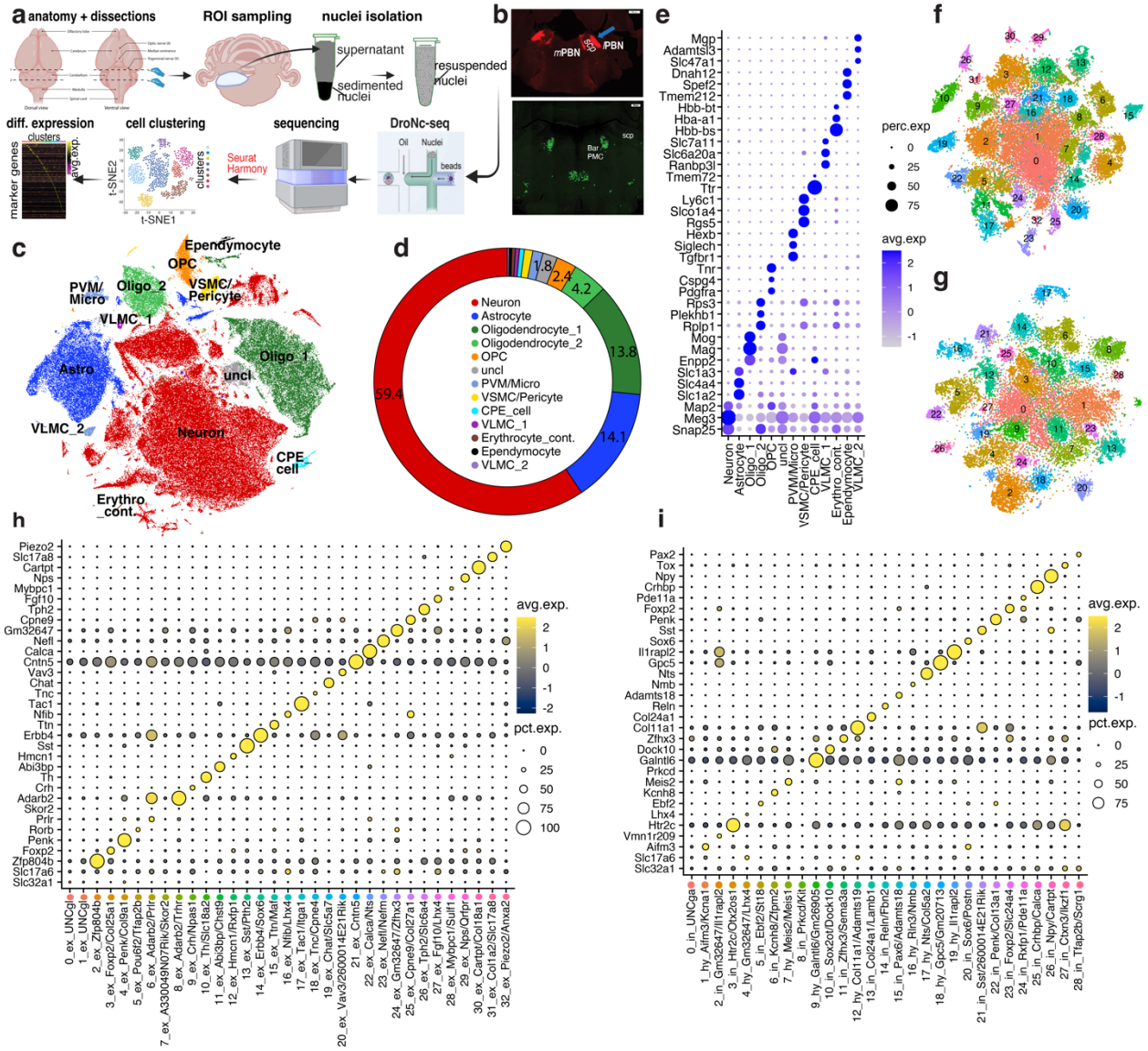
a
anatomy + dissections
ROI sampling
nuclei isolation
supernatant
sedimented nuclei
resuspended nuclei
diff. expression
cell clustering
sequencing
DroNc-seq
Seurat Harmony
marker genes
clusters
avg.exp.
t-SNE1
t-SNE2
Oil
Nuclei
beads
b
mPBN
PBN
scp
Bar PMC
c
Ependymocyte
OPC
PVM/ Micro
Oligo_2
VSMC/ Pericyte
VLMC_1
Astro
Oligo_1
uncl
VLMC_2
Neuron
CPE cell
Erythro _cont.
d
Neuron
Astrocyte
Oligodendrocyte_1
Oligodendrocyte_2
OPC
uncl
PVM/Micro
VSMC/Pericyte
CPE_cell
VLMC_1
Erythrocyte_cont.
Ependymocyte
VLMC_2
59.4
14.1
13.8
4.2
2.4
1.8
e
perc.exp
avg.exp
f
g
h
avg.exp.
pct.exp.
i
avg.exp.
pct.exp.

Figure 1

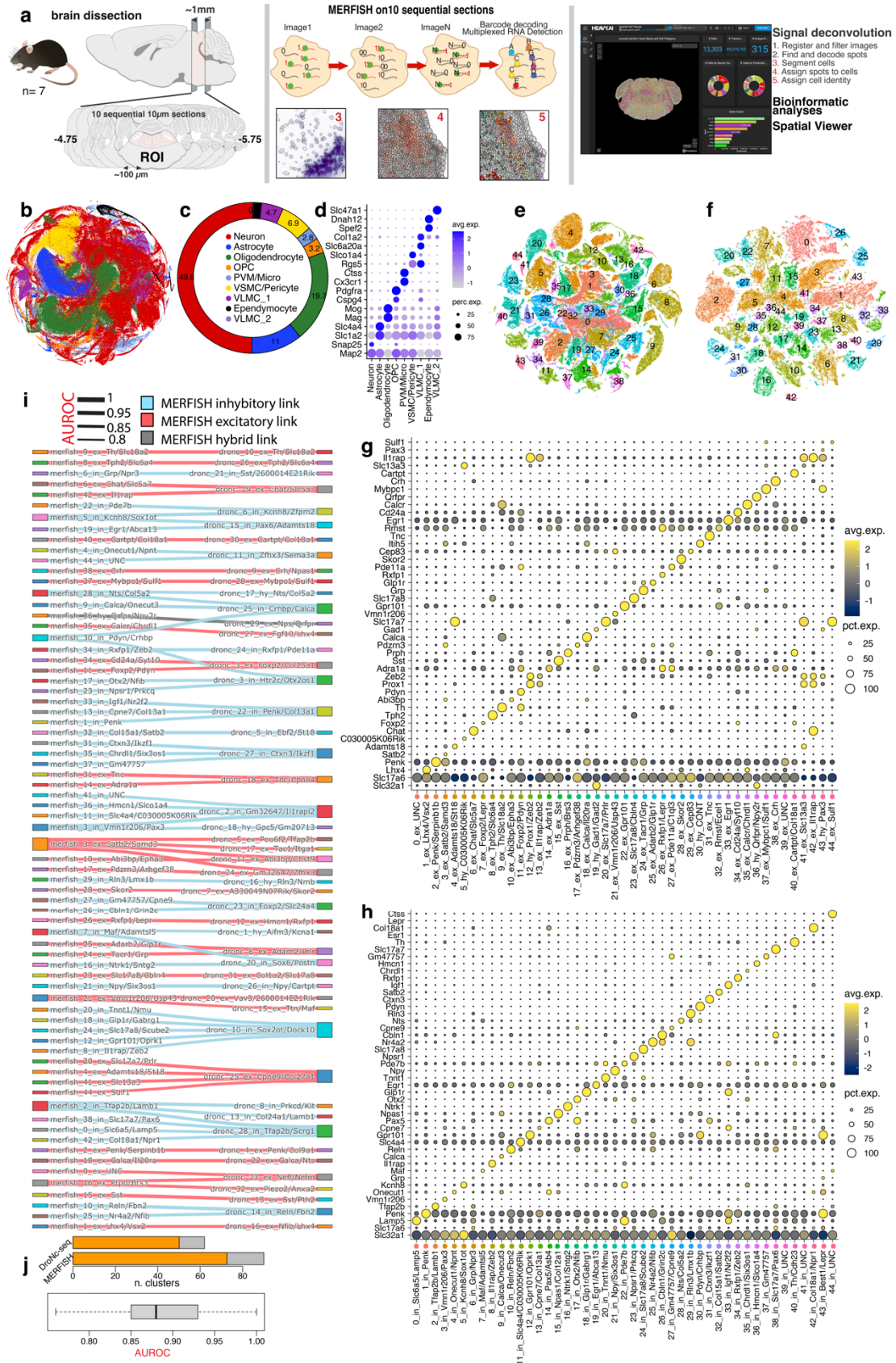
a
brain dissection
~1mm
n= 7
10 sequential 10μm sections
-4.75
-5.75
ROI
~100 μm
MERFISH on10 sequential sections
Image1
Image2
ImageN
Barcode decoding
Multiplexed RNA Detection
Signal deconvolution
1. Register and filter images
2. Find and decode spots
3. Segment cells
4. Assign spots to cells
5. Assign cell identity
Bioinformatic analyses
Spatial Viewer
b
c
Neuron
Astrocyte
Oligodendrocyte
OPC
PVM/Micro
VSMC/Pericyte
VLMC_1
Ependymocyte
VLMC_2
d
avg.exp.
perc.exp.
e
f
i
AUROC
MERFISH inhybitory link
MERFISH excitatory link
MERFISH hybrid link
g
avg.exp.
pct.exp.
h
avg.exp.
pct.exp.
j
DroNc-seq
MERFISH
n. clusters
AUROC

Figure 2

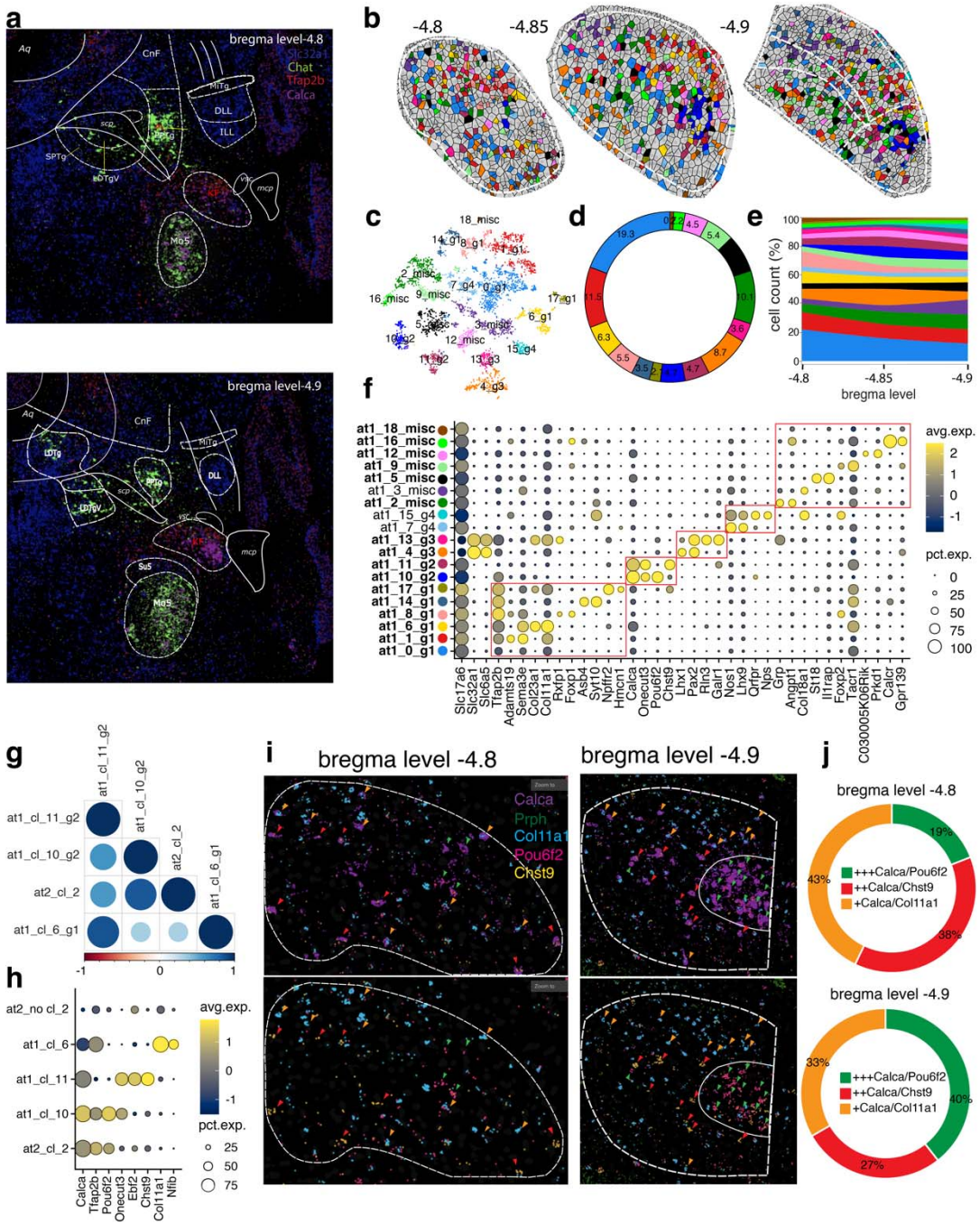
a
bregma level-4.8
Slc32a1
Chat
Tfap2b
Calca
bregma level-4.9
b
-4.8
-4.85
-4.9
c
d
e
cell count (%)
bregma level
f
avg.exp.
pct.exp.
g
h
avg.exp.
pct.exp.
i
bregma level -4.8
bregma level -4.9
Calca
Prph
Col11a1
Pou6f2
Chst9
j
bregma level -4.8
+++Calca/Pou6f2
++Calca/Chst9
+Calca/Col11a1
19%
43%
38%
bregma level -4.9
+++Calca/Pou6f2
++Calca/Chst9
+Calca/Col11a1
33%
40%
27%

Figure 3

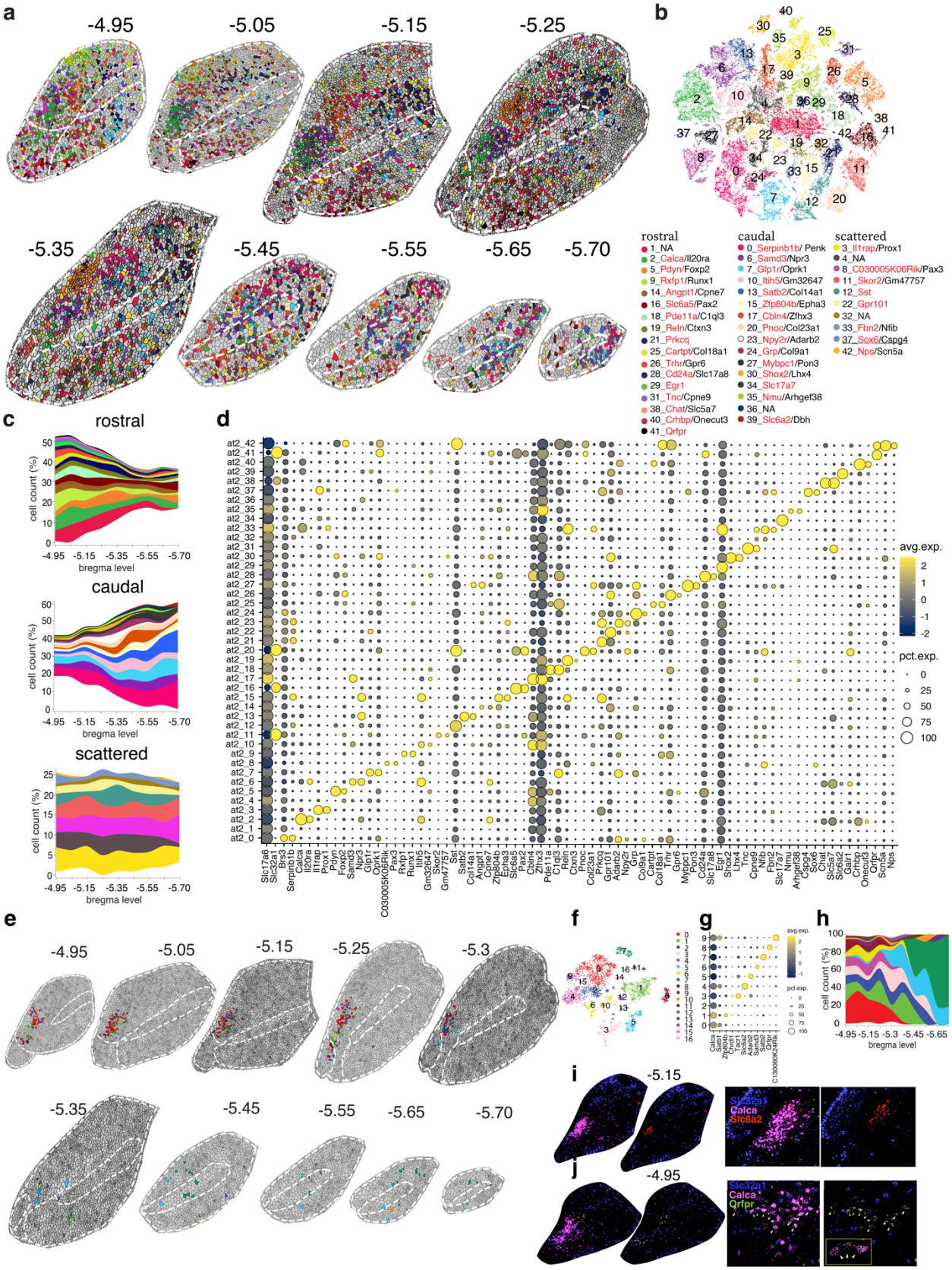
a
-4.95
-5.05
-5.15
-5.25
-5.35
-5.45
-5.55
-5.65
-5.70
b
rostral
1_NA
2_Calca/Il20ra
5_Pdyn/Foxp2
9_Rxfp1/Runx1
14_Angpt1/Cpne7
16_Slc6a5/Pax2
18_Pde11a/C1ql3
19_Reln/Ctxn3
21_Prkcq
25_Cartpt/Col18a1
26_Trhr/Gpr6
28_Cd24a/Slc17a8
29_Egr1
31_Tnc/Cpne9
38_Chat/Slc5a7
40_Crhbp/Onecut3
41_Qrfpr
caudal
0_Serpinb1b/ Penk
6_Samd3/Npr3
7_Glp1r/Oprk1
10_Itih5/Gm32647
13_Satb2/Col14a1
15_Zfp804b/Epha3
17_Cbln4/Zfhx3
20_Pnoc/Col23a1
23_Npy2r/Adarb2
24_Grp/Col9a1
27_Mybpc1/Pon3
30_Shox2/Lhx4
34_Slc17a7
35_Nmu/Arhgef38
36_NA
39_Slc6a2/Dbh
scattered
3_Il1rap/Prox1
4_NA
8_C030005K06Rik/Pax3
11_Skor2/Gm47757
12_Sst
22_Gpr101
32_NA
33_Fbn2/Nfib
37_Sox6/Cspg4
42_Nps/Scn5a
c
rostral
caudal
scattered
cell count (%)
bregma level
d
avg.exp.
pct.exp.
e
f
g
h
i
j
Slc32a1
Calca
Slc6a2
Qrfpr

Figure 4

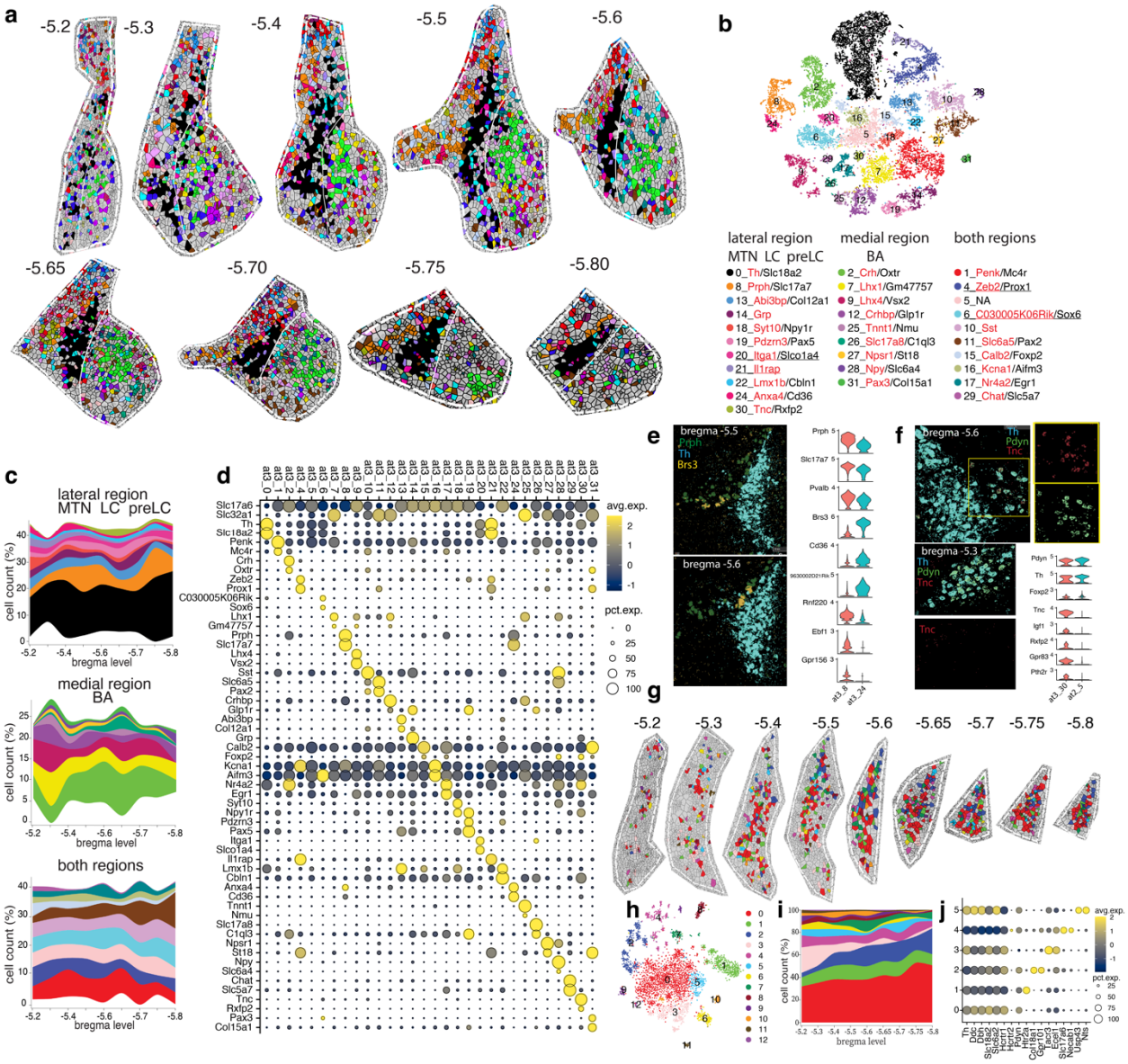
a
-5.2
-5.3
-5.4
-5.5
-5.6
-5.65
-5.70
-5.75
-5.80
b
lateral region
MTN LC preLC
medial region
BA
both regions
0_Th/Slc18a2
8_Prph/Slc17a7
13_Abi3bp/Col12a1
14_Grp
18_Syt10/Npy1r
19_Pdzrn3/Pax5
20_Itga1/Slco1a4
21_Il1rap
22_Lmx1b/Cbln1
24_Anxa4/Cd36
30_Tnc/Rxfp2
2_Crh/Oxtr
7_Lhx1/Gm47757
9_Lhx4/Vsx2
12_Crhbp/Glp1r
25_Tnnt1/Nmu
26_Slc17a8/C1ql3
27_Npsr1/St18
28_Npy/Slc6a4
31_Pax3/Col15a1
1_Penk/Mc4r
4_Zeb2/Prox1
5_NA
6_C030005K06Rik/Sox6
10_Sst
11_Slc6a5/Pax2
15_Calb2/Foxp2
16_Kcna1/Aifm3
17_Nr4a2/Egr1
29_Chat/Slc5a7
c
lateral region
MTN LC preLC
medial region
BA
both regions
cell count (%)
bregma level
d
avg.exp.
pct.exp.
e
bregma -5.5
Prph
Th
Brs3
bregma -5.6
f
bregma -5.6
Th
Pdyn
Tnc
bregma -5.3
g
-5.2
-5.3
-5.4
-5.5
-5.6
-5.65
-5.7
-5.75
-5.8
h
i
cell count (%)
bregma level
j
avg.exp.
pct.exp.

Figure 5

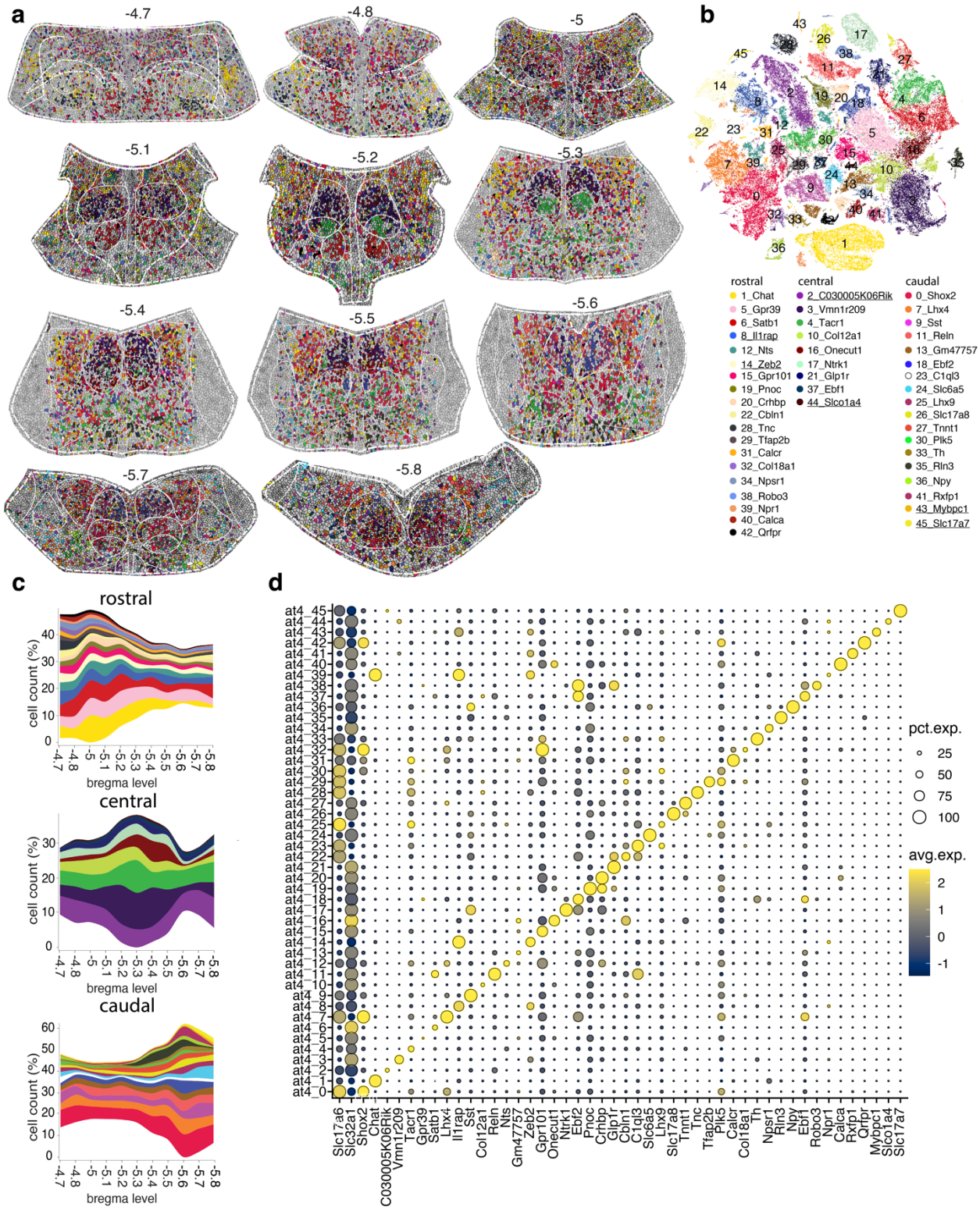
a
-4.7
-4.8
-5
-5.1
-5.2
-5.3
-5.4
-5.5
-5.6
-5.7
-5.8
b
rostral
1_Chat
5_Gpr39
6_Satb1
8_Il1rap
12_Nts
14_Zeb2
15_Gpr101
19_Pnoc
20_Crhbp
22_Cbln1
28_Tnc
29_Tfap2b
31_Calcr
32_Col18a1
34_Npsr1
38_Robo3
39_Npr1
40_Calca
42_Qrfpr
central
2_C030005K06Rik
3_Vmn1r209
4_Tacr1
10_Col12a1
16_Onecut1
17_Ntrk1
21_Glp1r
37_Ebf1
44_Slco1a4
caudal
0_Shox2
7_Lhx4
9_Sst
11_Reln
13_Gm47757
18_Ebf2
23_C1ql3
24_Slc6a5
25_Lhx9
26_Slc17a8
27_Tnnt1
30_Plk5
33_Th
35_Rln3
36_Npy
41_Rxfp1
43_Mybpc1
45_Slc17a7
c
rostral
central
caudal
cell count (%)
bregma level
d
pct.exp.
25
50
75
100
avg.exp.
2
1
0
-1

Figure 6

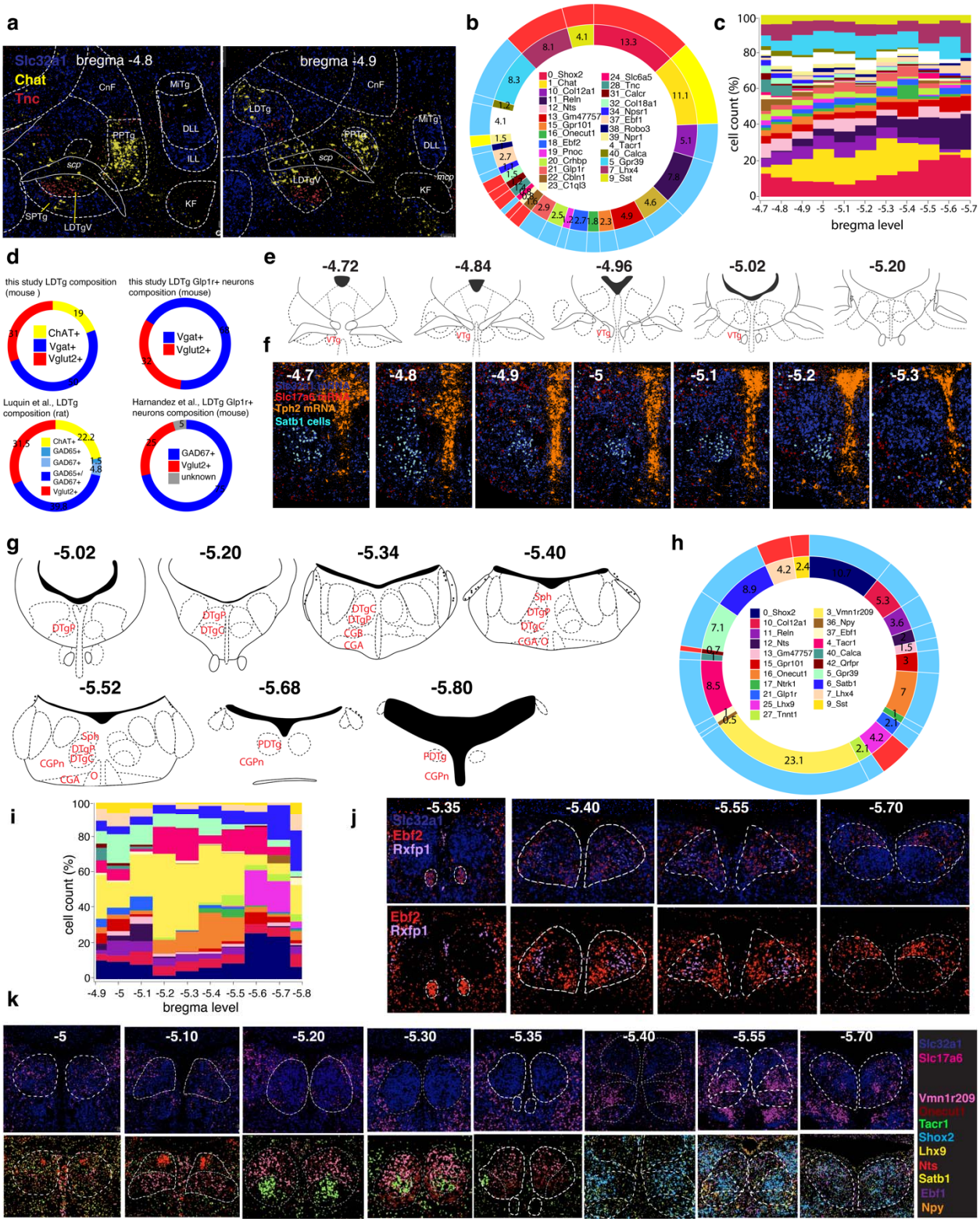
a
Slc32a1
Chat
Tnc
bregma -4.8
bregma -4.9
CnF
MiTg
DLL
ILL
PPTg
scp
KF
SPTg
LDTgV
LDTg
mcp
b
0_Shox2
1_Chat
10_Col12a1
11_Reln
12_Nts
13_Gm47757
15_Gpr101
16_Onecut1
18_Ebf2
19_Pnoc
20_Crhbp
21_Glp1r
22_Cbln1
23_C1ql3
24_Slc6a5
28_Tnc
31_Calcr
32_Col18a1
34_Npsr1
37_Ebf1
38_Robo3
39_Npr1
4_Tacr1
40_Calca
5_Gpr39
7_Lhx4
9_Sst
c
cell count (%)
bregma level
d
this study LDTg composition (mouse)
ChAT+
Vgat+
Vglut2+
this study LDTg Glp1r+ neurons composition (mouse)
Vgat+
Vglut2+
Luquin et al., LDTg composition (rat)
ChAT+
GAD65+
GAD67+
GAD65+/ GAD67+
Vglut2+
Harnandez et al., LDTg Glp1r+ neurons composition (mouse)
GAD67+
Vglut2+
unknown
e
-4.72
-4.84
-4.96
-5.02
-5.20
VTg
f
-4.7
-4.8
-4.9
-5
-5.1
-5.2
-5.3
Slc17a6 mRNA
Tph2 mRNA
Satb1 cells
g
-5.02
-5.20
-5.34
-5.40
-5.52
-5.68
-5.80
DTgP
DTgC
CGB
CGA
Sph
O
CGPn
PDTg
h
0_Shox2
10_Col12a1
11_Reln
12_Nts
13_Gm47757
15_Gpr101
16_Onecut1
17_Ntrk1
21_Glp1r
25_Lhx9
27_Tnnt1
3_Vmn1r209
36_Npy
37_Ebf1
4_Tacr1
40_Calca
42_Qrfpr
5_Gpr39
6_Satb1
7_Lhx4
9_Sst
i
cell count (%)
bregma level
j
-5.35
-5.40
-5.55
-5.70
Slc32a1
Ebf2
Rxfp1
k
-5
-5.10
-5.20
-5.30
-5.35
-5.40
-5.55
-5.70
Slc32a1
Slc17a6
Vmn1r209
Onecut1
Tacr1
Shox2
Lhx9
Nts
Satb1
Ebf1
Npy

Figure 7

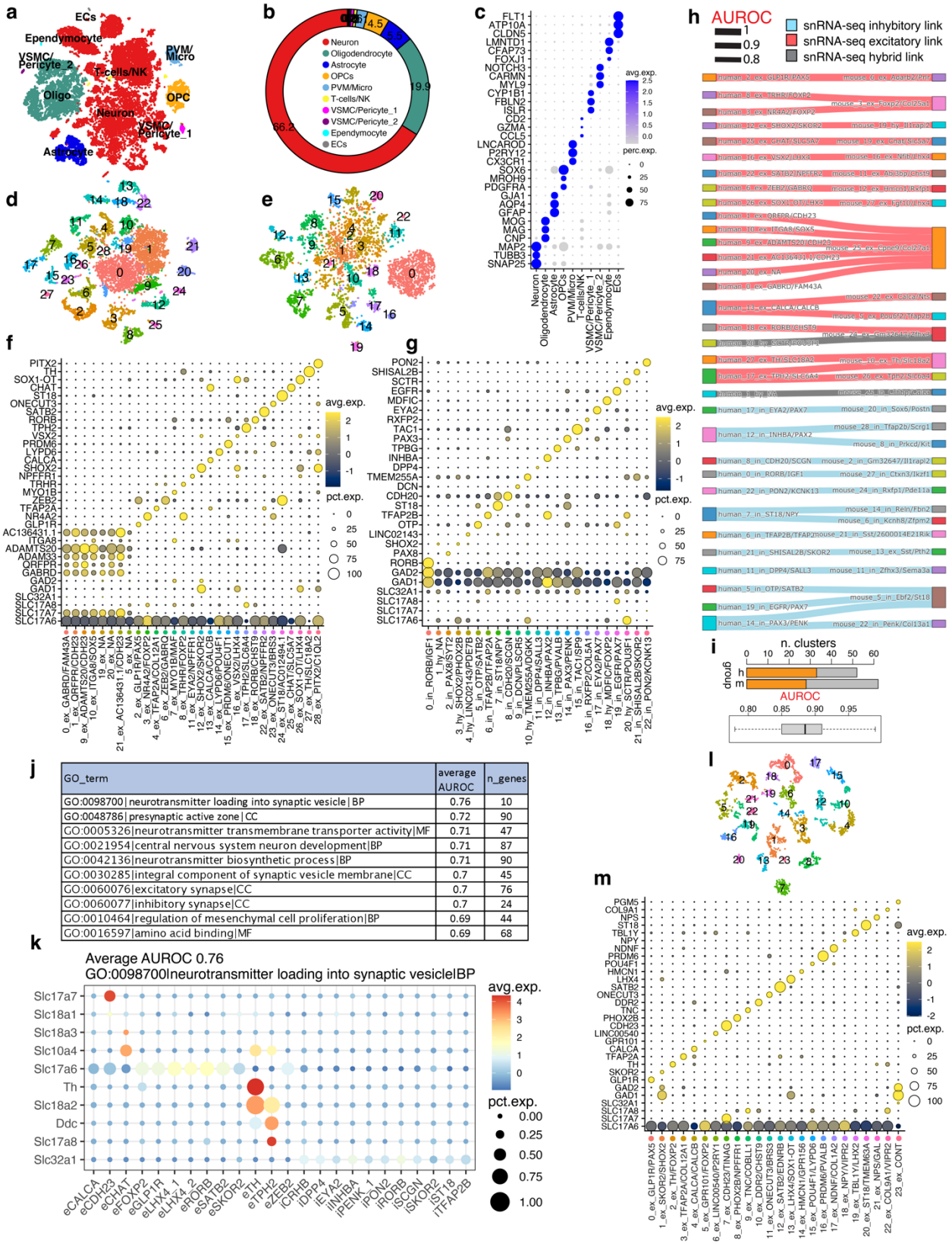

GO_term	average AUROC	n_genes
GO:0098700|neurotransmitter loading into synaptic vesicle|BP	0.76	10
GO:0048786|presynaptic active zone|CC	0.72	90
GO:0005326|neurotransmitter transmembrane transporter activity|MF	0.71	47
GO:0021954|central nervous system neuron development|BP	0.71	87
GO:0042136|neurotransmitter biosynthetic process|BP	0.71	90
GO:0030285|integral component of synaptic vesicle membrane|CC	0.7	45
GO:0060076|excitatory synapse|CC	0.7	76
GO:0060077|inhibitory synapse|CC	0.7	24
GO:0010464|regulation of mesenchymal cell proliferation|BP	0.69	44
GO:0016597|amino acid binding|MF	0.69	68

Figure 8

Fig1. DroNc-seq transcriptional profile of the dPnTg. a) Experimental workflow summarized in 5 main steps: dissections, nuclei isolation, DroNc-seq, sequencing, and bioinformatic analyses. **b**) Image illustrating the two dissection strategies relying on the visualization of PB (top) and Bar (bottom). **c)** t-SNE plot of 148,433 nuclei color-coded according to the legend in panel d. **d)** Donut plot representing the fraction (%) of each cell type identified. **e**) Dot plot of 35 cell marker genes (y-axis) that univocally identify each cell type (x-axis). 3 marker genes were plotted for all cell types except for CPE-cells, where only the top 2 were used. **f**-**g**) t-SNE plots showing 35,861 nuclei from the "excitatory" group (f) and 24,526 nuclei from the "inhibitory" group (g) color-coded by cell cluster. The top marker genes specify the identity of each cluster as per panels h and i, respectively. **h**-**i**) Dot plot illustrating the expression level of the top marker gene for the "excitatory" (h) and "inhibitory" (i) neuronal groups. All differentially expressed genes in the dot plot have an average log fold-change >0.25 and an adjusted p-value <0.01. Test used: *Wilcoxon Rank Sum two-sided Bonferroni-corrected Test*. lPBN/ mPBN parabrachial nucleus lateral/ medial divisions; Bar, Barrington's nucleus; scp, superior cerebellar peduncle; t-SNE, t-distributed Stochastic Neighbor Embedding; OPC, oligodendrocyte progenitor cell; PVM/Micro, perivascular macrophages /microglia; VSMC, vascular smooth muscle cells; CPE cells, choroid plexus epithelial cells; VLMC1/ 2, vascular and leptomeningeal cell type 1/ 2.

Fig2. MERFISH transcriptional profile of the dPnTg and correspondence between MERFISH and DroNc-seq data. a) Experimental workflow summarized in 5 main steps: dissection, MERFISH assay, signal deconvolution, bioinformatic analyses, and data visualization. **b**) t-SNE plot of 685,289 cells color-coded according to the legend in panel c. **c**) Donut plot depicting the fraction (%) of each cell type identified. **d**) Dot plot of 17 cell markers (y-axis) that univocally identify each cell type (x-axis). For each cell type, two markers were plotted, except for VLMC types I and II, where one marker was used. **e**-**f**) t-SNE of 231,103 cells from the "excitatory" group (e) and 110,332 cells from the "inhibitory" group (f) color-coded by cell cluster. The top two marker genes specify the identity of each cluster as per panels g and h, respectively. **g**-**h**) Dot plot of the expression level of the top marker gene for the "excitatory" (g) and "inhibitory" (h) neuronal clusters. **i**) Sankey plot depicting the cluster correspondence between MERFISH and DroNc-seq datasets. The thickness of the line reflects the AUROC score. **j**) Top: stacked bar plot showing the number of clusters with a match (orange) over the total clusters (grey) identified by MERFISH and DroNc-seq approaches. Bottom: boxplot showing the AUROC scores distribution. Highlighted in black is the median. Black circles indicate outliers. All differentially expressed genes in the dot plot have an average log fold-change >0.25 and an adjusted p-value <0.01. Test used: *Wilcoxon Rank Sum two-sided Bonferroni-corrected Test*. Source Data is provided as a Source Data file. t-SNE, t-distributed Stochastic Neighbor Embedding; OPC, oligodendrocyte progenitor cell; PVM/Micro, perivascular macrophages /microglia; VSMC, vascular smooth muscle cells; CPE cells, choroid plexus cells; VLMC1/ 2, vascular and leptomeningeal cell type 1/ 2; AUROC, area under the receiver operator characteristic curve.

Fig3. Spatially-resolved neuronal atlas of the KF a) Overlay of Franklin-Paxinos atlas anatomic boundaries on MERFISH image depicting *Slc32a1*, *Chat*, *Tfap2b,* and *Calca* transcripts. **b**) Voronoi plots depicting KF cells across 3 bregma levels. **c**) t-SNE plot of 4,554 neurons from the KF. **d**) Donut plot showing the fraction (%) of each neuronal cluster of the KF. **e**) Stacked area chart showing each cluster's cell frequency (*cluster trajectory*) across 3 bregma levels. **f**) Dot plot showing the top 3 markers for each cluster. Red boxes indicate the five groups. Clusters displayed by the Voronoi, t-SNE, donut plot, and stacked area chart are color-coded according to the legend in panel f. Glia/ non-neuronal cells are in grey. **g**) Heatmap depicting the Pearson's *r* correlation coefficient of the average expression of 315 genes for all

possible combinations of the PB cluster at2_2, KF clusters at1_6, at1_10, and at1_11. **h**) Dot Plot of marker genes specific for PB cluster at2_2, all PB clusters except at2_2, KF clusters at1_6, at1_10, and at1_11. **i**) MERFISH images depicting *Calca*, *Prph*, *Col11a1*, *Pou6f2*, and *Chst9* transcripts in the KF at bregma levels -4.8 and -4.9. Green, red, and orange arrows represent high Calca (*Calca*+++/*Pou6f2,* KF cluster at1_10), medium Calca (*Calca*++/ *Chst9,* KF cluster at1_11), and low Calca (*Calca*+/*Col11a1,* KF cluster at1_6) neuronal clusters, respectively. **j**) Donut plot depicting the fraction of *Calca*+ neuronal clusters (clusters at1_6, at1_10, and at1_11) at bregma level -4.8 and -4.9 of the KF. The cluster percentage in plots refers to the images in panel i. All differentially expressed genes in the dot plot have an average log fold-change >0.25 and an adjusted p-value <0.01. Test used: *Wilcoxon Rank Sum two-sided Bonferroni-corrected Test*.

Fig4. Spatially-resolved neuronal atlas of the PB. a) Voronoi plots depicting PB cells across 9 sequential MERFISH sections from -4.95 to -5.70 bregma level. **b**) t-SNE plot of 79,413 neurons. **c**) Stacked area charts showing each cluster's cell frequency (*cluster trajectory*) across all 9 bregma levels. Clusters displayed by the Voronoi, t-SNE, and stacked area chart are color-coded according to the legend in panel b. Glia/ non-neuronal cells are in grey. **d**) Dot plot of the top 2 markers for each cluster. Neuronal cells are color-coded according to cluster number as per legend in panel b. Glia and non-neuronal cells are in grey. **e**) Voronoi plots representing neurons from PB cluster at2_2 across 10 sequential coronal sections from bregma level -4.95 to -5.75. **f**) t-SNE plot representing 4,504 neurons. **g**) Dot plot depicting the *Calca* gene and the top marker for each *Calca*+ subcluster. **h**) Stacked area chart showing the *cluster trajectory* across the ten sequential MERFISH sections in panel e. Clusters displayed by the Voronoi, t-SNE, and stacked area chart are color-coded according to the legend in panel f. Glia/ non-neuronal cells are in grey. **i**) Left: MERFISH image of *Slc32a1*, *Calca,* and *Slc6a2* transcripts in the PB complex at bregma level -5.15. Right: enlarged view of the *Calca*+ cluster 4. **j**) Left: MERFISH image of *Slc32a1*, *Calca,* and *Qrfpr* transcripts in the PB complex at bregma level -4.95. Right: enlarged view of the *Calca*+ cluster 8. All differentially expressed genes in the dot plot have an average log fold-change >0.25 and an adjusted p-value <0.01. Test used: *Wilcoxon Rank Sum two-sided Bonferroni-corrected Test*.

Fig5. Spatially-resolved neuronal atlas of the MTN, pre-LC, LC, and Bar. a) Voronoi plots depicting cells of a ROI that includes MTN, pre-LC, LC, and Bar across 9 sequential sections, from -5.2 to -5.8 bregma level. **b**) t-SNE plot of 22,358 neurons. **c**) Stacked area chart showing each cluster's cell frequency (*cluster trajectory*) across all 9 MERFISH sections. Clusters displayed by the Voronoi, t-SNE, and stacked area chart are color-coded according to the legend in panel b. Glia/ non-neuronal cells are in grey. **d**) Dot plot of the top two markers for each cluster. **e**) Left: MERFISH image showing the spatial distribution of *Prph*, *Th,* and *Brs3* at bregma levels -5.5 and -5.6. Right: violin plots depicting the average expression level (y-axis) of 9 genes in clusters at3_8 and at3_24 (x-axis). **f**) Left: MERFISH image showing the spatial distribution for *Th*, *Pdyn,* and *Tnc* in bregma levels -5.6 and -5.3 in the pre-LC (top) and LPBD (bottom). Right: violin plots depicting the expression level (y-axis) of eight genes in clusters at3_30 (pre-LC) and at2_5 (LPBD) (x-axis). **g**) Voronoi plots depicting LC noradrenergic neurons across 9 sequential MERFISH sections from -5.2 to -5.8 bregma level. **h**) t-SNE plot of 4,074 noradrenergic neurons **i**) Stacked area chart showing each cluster's cell frequency (*cluster trajectory*) across 9 sequential MERFISH sections in panel g. Clusters displayed by the Voronoi, t-SNE, and stacked area chart are color-coded according to the legend in panel h. Glia/ non-neuronal cells are in grey. **j**) Dot plot depicting *Th*, *Ddc*, *Dbh*, *Slc18a2*, *Slc6a2, Hcrtr1,* and *Hcrtr2* genes and the top 2 marker genes for each subcluster. All differentially expressed genes in the dot plot have an average log fold-change >0.25 and an adjusted p-value <0.01. Test used: *Wilcoxon Rank Sum two-sided Bonferroni-corrected Test*.

Fig6. Spatially-resolved neuronal atlas of LDTg, DTg, VTg, Sph, NI, CGA, CGB, and CGPn. **a**) Voronoi plots depicting cells of a ROI that includes LDTg, DTg, VTg, Sph, NI, CGA, CGB, and CGPn across 11 sequential sections from -4.7 to -5.8 bregma level. **b**) t-SNE plot of 120,182 neurons. **c**) Stacked area charts showing the *cluster trajectory* across all 11 bregma levels. Clusters displayed by the Voronoi, t-SNE, and stacked area chart are color-coded according to the legend in panel b. Glia/ non-neuronal cells are in grey. **d**) Dot plot of the top marker for each cluster. All differentially expressed genes in the dot plot have an average log fold-change >0.25 and an adjusted p-value <0.01. Test used: *Wilcoxon Rank Sum two-sided Bonferroni-corrected Test*. Source Data are provided as Source Data files.

Fig7. A detailed characterization of the LDTg, VTg, DTg, and Sph. a) Overlay of Franklin-Paxinos atlas anatomic boundaries on MERFISH image depicting *Slc32a1*, *Chat*, and *Tnc* transcripts. **b**) Donut plots: the inner plot shows the overall contribution (%) of each cluster to the total LDTg/ LDTgV neurons; the outer plot classifies each cluster as glutamatergic (red), GABAergic (light blue) and cholinergic (yellow). **c**) Stacked area charts of the LDTg/ LDTgV cluster trajectory. Clusters are color-coded according to the legend in panel b. **d**) Left: donut plot showing the LDTg cell partition in glutamatergic (red), GABAergic (blue), and cholinergic (yellow) in this study and as reported by Luquin et al. Right: estimation of *Glp1r*+/*Vgat*+ and *Glp1+r*/*Vglut2*+ cells in mouse LDTg by this study and as reported by Hernandez et al. **e**) Schematic from the Paxinos atlas showing the VTg anatomical location. **f**) MERFISH image showing cluster at4_6 (VTg neurons; cyan polygons) along with *Slc32a1*, *Slc17a6,* and *Tph2* transcripts. **g**) Schematic from the Franklin-Paxinos atlas showing the DTg, Sph, NI, CGA, and CGB anatomical location from -5.02 to -5.8 bregma level. For panels e and g, abbreviations refer to Table 1. **h**) Donut plots: the inner plot shows the overall contribution (%) of each cluster to the total DTg neurons; the outer plot classifies each cluster as glutamatergic (red) and GABAergic (light blue). **i**) Stacked area charts of the DTg cluster trajectory. Clusters are color-coded according to the legend in panel h. **j**) Overlay of Franklin-Paxinos atlas anatomic boundaries on MERFISH images depicting *Vgat, Ebf2,* and *Rfxfp1* (top) and *Ebf2* and *Rfxp1* marker genes (bottom) in the Sph. **k**) Overlay of Franklin-Paxinos atlas anatomic boundaries on MERFISH images depicting *Vgat* and *Vglut2* (top) and 9 marker genes (bottom) in the DTg across the same rostrocaudal levels. Legend is on the right side of both panels. Source Data are provided as Source Data files.

Fig8. snRNA-seq transcriptional profile of the human dPnTg and correspondence between human snRNA-seq and mouse DroNc-seq data. a) t-SNE plot of 24,977 nuclei. **b**) Donut plot depicting the fraction (%) of each cell type identified. Color-coded legend for panels a and b is in panel b. **c**) Dot plot of 30 cell markers (y-axis) that univocally identify each cell type (x-axis). For each cell type, 3 markers were plotted. **d**-**e**) t-SNE plots of 8,632 neuronal nuclei from the "excitatory" group (d) and 6,221 neuronal nuclei from the "inhibitory" group (e) color-coded by cell cluster according to legends in panels f and g, respectively. **f**-**g**) Dot plots displaying the expression level of the top marker gene for the "excitatory" (f) and "inhibitory" (g) neuronal clusters. The top 2 marker genes specify the identity of each cluster. **h**) Sankey plot depicting the clusters correspondence between human snRNA-seq and mouse DroNc-seq datasets in the dPnTg. The thickness of the line reflects the AUROC score. **i**) Top: stacked bar plot showing the number of clusters with a match (orange) over the total clusters (grey) identified by snRNA-seq and DroNc-seq approaches. Bottom: boxplot showing the AUROC scores distribution. Highlighted in black is the median. Black circles indicate outliers. **j**) Table representing the top 10 GO gene sets contributing to cluster replicability. **k**) Dot plot displaying the expression (z-score) of genes relative to GO:0098700. The gene expression is first averaged and scaled in each dataset independently, and the plotted values are obtained by

averaging across datasets. Matches are defined by a joint label that uses one of the top 2 marker genes from human clusters. **l**) t-SNE plot of 3,384 neuronal nuclei derived exclusively from human PB dissections. **m**) Dot plots displaying each cluster's top marker gene expression level. All differentially expressed genes in the dot plot have an average log fold-change >0.25 and an adjusted p-value <0.01. Test used: *Wilcoxon Rank Sum two-sided Bonferroni-corrected Test*. Source Data is provided as a Source Data file. t-SNE, t-distributed Stochastic Neighbor Embedding; OPC, oligodendrocyte progenitor cell; PVM/Micro, perivascular macrophages /microglia; VSMC, vascular smooth muscle cell; NK, natural killer cell; ECs, endothelial cells; AUROC, area under the receiver operator characteristic curve, h, *homo sapiens*; m, *mus musculus*.